

REPORT DOCUMENTATION PAGE				Form Approved OMB No. 0704-0188	
<p>The public reporting burden for this collection of information is estimated to average 1 hour per response, including the time for reviewing instructions, searching existing data sources, gathering and maintaining the data needed, and completing and reviewing the collection of information. Send comments regarding this burden estimate or any other aspect of this collection of information, including suggestions for reducing the burden, to the Department of Defense, Executive Services and Communications Directorate (0704-0188). Respondents should be aware that notwithstanding any other provision of law, no person shall be subject to any penalty for failing to comply with a collection of information if it does not display a currently valid OMB control number.</p> <p><b>PLEASE DO NOT RETURN YOUR FORM TO THE ABOVE ORGANIZATION.</b></p>					
1. REPORT DATE (DD-MM-YYYY) 08-02-2012		2. REPORT TYPE Journal Article		3. DATES COVERED (From - To)	
4. TITLE AND SUBTITLE Long Island Sound Coastal Observatory: Assessment of Above-Water Radiometric Measurement Uncertainties Using Collocated Multi and Hyper-Spectral Systems				5a. CONTRACT NUMBER	
				5b. GRANT NUMBER	
				5c. PROGRAM ELEMENT NUMBER 0601153N	
6. AUTHOR(S) T. Harmel, A. Gilerson, S. Hlaing, A. Tonizzo, T. Legbandt, Alan Weidemann, Robert Amone, S. Ahmed				5d. PROJECT NUMBER	
				5e. TASK NUMBER	
				5f. WORK UNIT NUMBER 73-9343-01-5	
7. PERFORMING ORGANIZATION NAME(S) AND ADDRESS(ES) Naval Research Laboratory Oceanography Division Stennis Space Center, MS 39529-5004				8. PERFORMING ORGANIZATION REPORT NUMBER NRL/JA/7330-11-0884	
9. SPONSORING/MONITORING AGENCY NAME(S) AND ADDRESS(ES) Office of Naval Research One Liberty Center 875 North Randolph Street, Suite 1425 Arlington, VA 22203-1995				10. SPONSOR/MONITOR'S ACRONYM(S) ONR	
				11. SPONSOR/MONITOR'S REPORT NUMBER(S)	
12. DISTRIBUTION/AVAILABILITY STATEMENT Approved for public release, distribution is unlimited.					
20120213039					
13. SUPPLEMENTARY NOTES					
<b>14. ABSTRACT</b> <p>The Long Island Sound Coastal Observational platform (LISCO) near Northport, New York, has been recently established to support validation of ocean color radiometry (OCR) satellite data. LISCO is equipped with collocated multispectral, SeaPRISM, and hyperspectral, HyperSAS, above-water systems for OCR measurements. This combination offers the potential for improving validation activities of current and future OCR satellite missions, as well as for satellite intercomparisons and spectral characterization of coastal waters. Results of measurements made by both the multi and hyperspectral instruments, in operation since October 2009, are presented, evaluated and their associated uncertainties quantified based on observations for a period of over a year. Multi- and hyperspectral data processing as well as the data quality analysis are described and their uncertainties evaluated. The quantified intrinsic uncertainties of HyperSAS data exhibit satisfactory values, less than 5% over a large spectral range, from 340 to 740 nm, and over a large range of diurnal daylight conditions, depending on the maximum sun elevation at the solar noon. Intercomparisons between HyperSAS and SeaPRISM data revealed that an overcorrection of the sun glint effect in the current SeaPRISM processing induces errors, which are amplified through the whole data processing, especially at the shorter wavelengths. The spectral-averaged uncertainties can be decomposed as follows: (i) sun glint removal generates 2% uncertainty, (ii) sky glint removal generates strong uncertainties of the order of 15% mainly induced by sun glint overcorrection, (iii) viewing angle dependence corrections improve the data intercomparison by reducing the dispersion by 2%, (iv) normalization of atmospheric effects generates approximately 4% uncertainty. Based on this study, improvements of the sun glint correction are expected to significantly reduce the uncertainty associated with the data processing down to the level of 1%.</p>					
<b>15. SUBJECT TERMS</b> <p>water leaving radiance, ocean color radiometry, hyperspectral systems, optical remote sensing</p>					
16. SECURITY CLASSIFICATION OF:			17. LIMITATION OF ABSTRACT  UU	18. NUMBER OF PAGES  19	19a. NAME OF RESPONSIBLE PERSON Alan Weidemann
a. REPORT Unclassified	b. ABSTRACT Unclassified	c. THIS PAGE Unclassified			19b. TELEPHONE NUMBER (include area code) 228-688-6232

# Long Island Sound Coastal Observatory: Assessment of above-water radiometric measurement uncertainties using collocated multi and hyperspectral systems

Tristan Harmel,<sup>1</sup> Alexander Gilerson,<sup>1</sup> Soe Hlaing,<sup>1</sup> Alberto Tonizzo,<sup>1</sup> Tom Legbandt,<sup>1</sup> Alan Weidemann,<sup>2</sup> Robert Arnone,<sup>2</sup> and Samir Ahmed<sup>1,\*</sup>

<sup>1</sup>Optical Remote Sensing Laboratory, The City College of the City University of New York, New York City 10031, New York, USA

<sup>2</sup>Naval Research Laboratory, Stennis Space Center 39529, Mississippi, USA

\*Corresponding author: ahmed@ccny.cuny.edu

Received 28 March 2011; revised 29 June 2011; accepted 22 July 2011;  
posted 22 July 2011 (Doc. ID 144654); published 14 October 2011

The Long Island Sound Coastal Observational platform (LISCO) near Northport, New York, has been recently established to support validation of ocean color radiometry (OCR) satellite data. LISCO is equipped with collocated multispectral, SeaPRISM, and hyperspectral, HyperSAS, above-water systems for OCR measurements. This combination offers the potential for improving validation activities of current and future OCR satellite missions, as well as for satellite intercomparisons and spectral characterization of coastal waters. Results of measurements made by both the multi and hyperspectral instruments, in operation since October 2009, are presented, evaluated and their associated uncertainties quantified based on observations for a period of over a year. Multi- and hyperspectral data processing as well as the data quality analysis are described and their uncertainties evaluated. The quantified intrinsic uncertainties of HyperSAS data exhibit satisfactory values, less than 5% over a large spectral range, from 340 to 740 nm, and over a large range of diurnal daylight conditions, depending on the maximum sun elevation at the solar noon. Intercomparisons between HyperSAS and SeaPRISM data revealed that an overcorrection of the sun glint effect in the current SeaPRISM processing induces errors, which are amplified through the whole data processing, especially at the shorter wavelengths. The spectral-averaged uncertainties can be decomposed as follows: (i) sun glint removal generates 2% uncertainty, (ii) sky glint removal generates strong uncertainties of the order of 15% mainly induced by sun glint overcorrection, (iii) viewing angle dependence corrections improve the data intercomparison by reducing the dispersion by 2%, (iv) normalization of atmospheric effects generates approximately 4% uncertainty. Based on this study, improvements of the sun glint correction are expected to significantly reduce the uncertainty associated with the data processing down to the level of 1%. On the other hand, strong correlations between both datasets ( $R^2 > 0.96$ ) demonstrate the efficacy of the above-water retrieval concept and confirm that the collocated instrumentation constitutes an important aid to above-water data quality analysis, which makes LISCO a key element of the AERONET-OC network. © 2011 Optical Society of America

OCIS codes: 010.0010, 280.0280, 010.4450, 010.1320, 110.4234.

## 1. Introduction

Optical remote sensing of coastal waters from space is a basic requirement for effective monitoring of global water quality and assessing anthropogenic



impacts [1]. However, this task remains highly challenging because of the optical complexity of the atmosphere-water system in coastal areas. Atmospheric correction algorithms are applied to the total satellite signal to remove the contribution of the radiances reflected from the atmospheric and sea surface in order to produce estimates of the exact normalized water-leaving radiances,  $L_{WN}$ , the light vertically exiting the water mass under the hypothetical conditions of an overhead sun and normalized by the atmospheric transmittance [2–4]. This geophysical data processing is indeed very sensitive to the atmospheric and water composition [5–7] as well as to the calibration accuracy of the sensor [8,9]. The retrieved  $L_{WN}$ , which carries information on the water optical properties and the water composition, is therefore not error free, and its reliability needs to be assessed and validated against actual *in situ* measurements [10]. In connection with this, a worldwide effort is devoted to acquiring accurate *in situ* time series measurements in open ocean [11,12] and coastal waters [13].

In order to support present and future multi- and hyperspectral validation activities for ocean color radiometry satellites, as well as the development of new measurements and retrieval techniques for coastal waters, City College of New York along with the Naval Research Laboratory, Stennis, has established an observational platform, the Long Island Sound Coastal Observatory (LISCO) with multi- and hyperspectral radiometry capabilities. The multispectral measurements are obtained by an autonomous radiometer system called sea-viewing wide field-of-view sensor (SeaWiFS) photometer revision for incident surface measurements (SeaPRISM). This SeaPRISM system is part of the ocean color component of the NASA Aerosol Robotic Network (AERONET-OC). This network has been designed to support long-term satellite ocean color investigations through cross-site consistent and accurate measurements collected by autonomous radiometer systems deployed on offshore fixed platforms making measurements from above water [13–15]. LISCO complements these multispectral radiometric measurements by additional collocated and continuous hyperspectral measurements using a customized hyperspectral surface acquisition system (HyperSAS), which in addition to the spectral radiances measures the hyperspectral polarization properties of these coastal waters [16,17].

One of the major difficulties of above-water measurements is to correct observations for the impact of reflected sunlight (sun glint) and skylight (sky glint) components [14], which are also randomly fluctuating due to the effect of surface waves. These fluctuations introduce geophysical noise that needs to be removed from SeaPRISM and HyperSAS data. Based on the retrieval scheme developed for SeaPRISM [13,18], a hyperspectral-based procedure has been implemented to derive the normalized water-leaving radiance  $L_{WN}$  from HyperSAS

measurements. Thanks to the ability of LISCO SeaPRISM and HyperSAS to provide two collocated and coincident datasets, the consistency and the efficacy of the above-water data processing were assessed over a period of more than one year encompassing the full natural annual variability of atmospheric and water conditions.

In Section 2, below, the characteristics of the LISCO location and instrumentation are described, and the multi and hyperspectral above-water data correction algorithms detailed. The HyperSAS data quality process is also defined. In Section 3, the intrinsic uncertainties of HyperSAS are quantified, based on error propagation throughout the data processing. Then, LISCO data quality is assessed based on the respective data time series of the two collocated multi and hyperspectral systems. Inter-comparisons of HyperSAS and SeaPRISM direct measurement and derived products are carried out in order to quantify the uncertainty sources of above-water measurements. Finally, the dispersions observed between the two above-water datasets are discussed and improvements for limiting sources of uncertainty are delineated.

## 2. Long Island Sound Coastal Observatory Characteristics

### A. LISCO Location

The LISCO platform is located at approximately 3 km offshore in western Long Island Sound, New York. The coordinates of the site are N 40°57'16", W 73°20'30" [Fig. 1(a)]. The bathymetry in the immediate vicinity of the platform exhibits a plateau at around 13 meters depth [Fig. 1(b)]. It has been verified that this depth is deep enough to make the seabottom contribution to the water-leaving radiance negligible, as evidenced by the diffuse attenuation coefficient, which is typically close to  $0.3 \text{ m}^{-1}$ . LISCO is located in the area of western Long Island Sound that is usually moderately turbid with annual average concentrations of Chlorophyll-a and total suspended material of around  $12 \pm 4 \text{ mg m}^{-3}$  and  $3 \pm 0.5 \text{ g m}^{-3}$ , respectively, as estimated by Aurin *et al.* [19]. Based on some dozens of field cruises over one year in that region, this recent study characterizes LISCO waters as very productive and principally driven by phytoplankton biomass and associated detrital materials, rather than suspended sediments. Steady surface currents in the LISCO area are around  $0.3 \text{ m s}^{-1}$  on average according to NOAA HF Radar dataset.

### B. LISCO Instrumentation

The platform combines a multispectral SeaPRISM system (CIMEL ELECTRONIQUE, France) which is now part of the AERONET Ocean Color Network [13,15,20], with a collocated hyperspectral HyperSAS system (Satlantic, Canada). The instruments are positioned on a retractable tower on the LISCO platform with an elevation of 12 m. Both instruments



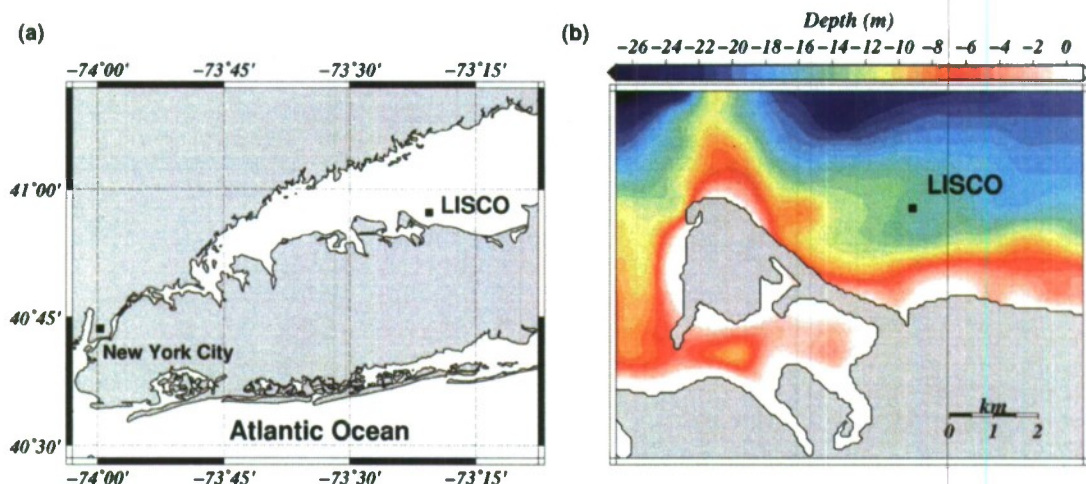


Fig. 1. (Color online) (a) LISCO map (LISCO coordinates  $N40.955^\circ$ ;  $W73.342^\circ$ ). (b) LISCO site bathymetry derived from the General Bathymetric Chart of the Oceans (GEBCO) dataset.

were installed in October 2009 and have been providing data since then.

The SeaPRISM system is made up of CE-318 sun photometers modified to meet requirements for above-water radiometry. The photometers perform radiance measurements with a FAFOV of  $1.2^\circ$  to determine the total radiance from the sea,  $L_T(\lambda, \theta, \varphi)$ , and the sky,  $L_s(\lambda, \theta', \varphi)$ , for the relative azimuth angle with respect to the sun  $\varphi$  and the respective viewing angles  $\theta$  and  $\theta'$  with  $\theta = \pi - \theta'$ . Thanks to the rotating feature of SeaPRISM, the azimuth  $\varphi$  is always set to  $90^\circ$  regardless of the sun position; the downwards viewing angle  $\theta$  is set to  $40^\circ$  from the nadir position. These values were determined in order to minimize both perturbations resulting from the sun glint of the sea surface [21] and the deployment of the superstructure itself or its shadow [15].

The SeaPRISM system configuration of LISCO performs ocean color measurements at the 413, 442, 491, 551, 668, 870 and 1018 nm center wavelengths. These center wavelengths were selected to be as close as possible to the bands of current ocean color radiometry satellite missions in order to support essential validation activities. In addition to these ocean color measurements, the regular data acquisitions of AERONET are also carried out, which permits accurate retrievals of the aerosol optical thickness and the fine-coarse aerosol mode fraction [22]. For all those types of measurements the integration time of the SeaPRISM radiometer is preset to 75 ms.

The hyperspectral measurements are made by a HyperSAS system, providing high precision hyperspectral measurements of total spectral radiance from the sea and the sky as well as downwelling spectral irradiance. The radiance and irradiance measurements of HyperSAS are carried out for 180 spectral channels regularly spaced between 305 and 905 nm. It has two radiance sensors, one looking down at the water, and the other looking skywards. They are mounted at the same location as the

SeaPRISM system and each have a FAFOV of  $3^\circ$ . Consequently, the sea target sensed by HyperSAS is larger than the SeaPRISM one. Indeed the intersection of the field of view with the sea surface forms an egg-shape of  $0.1 \text{ m}^2$  for SeaPRISM and  $0.7 \text{ m}^2$  for HyperSAS. These sensors provide the sea  $L_T(\lambda, \theta, \varphi)$  and the sky radiance  $L_s(\lambda, \theta', \varphi)$  for a fixed geometrical configuration with  $\theta = 40^\circ$  from the nadir view and pointing exactly westwards. As a result the relative azimuth  $\varphi$  is changing with respect to the sun position. Thus, SeaPRISM and HyperSAS point approximately at the same water target area when the sun is in the south, in other words around 12:00 LT. Each HyperSAS and SeaPRISM sea-viewing measurement sequence is executed every 30 min within plus or minus 4 h of 12:00 LT. The integration time of the HyperSAS radiometers is variable and is automatically adjusted according to the brightness of the scene. This parameter is around 2000 ms and 100 ms for typical sea and sky-radiance measurements, respectively.

The calibration of the SeaPRISM sun-photometer was carried out by the NASA AERONET group in accordance with the standard procedures of AERONET-OC. The recalibration performed in June 2011 (22 months after the initial calibration) showed an overall decrease of 2% in the radiometric sensitivity. The HyperSAS system calibration was carried out by Satlantic Inc. (Halifax, Canada) and checked at CCNY Optical Remote Sensing Lab. The recalibration by Satlantic Inc. of the HyperSAS system showed a radiometric stability, over a time period of approximately 15 months, of better than 1% for upwelling and downwelling radiance sensors and better than 0.5% for the irradiance sensor. SeaPRISM data are transferred by a satellite link to NASA, processed by the NASA AERONET group and posted on the NASA AERONET website. The near-real-time transmission of HyperSAS data is achieved by broadband cellular service to the CCNY server.



### 3. Above-Water Data Processing

#### A. Water-Leaving Radiance Retrieval Algorithm

The final geophysical product provided by HyperSAS or SeaPRISM system for their respective spectral bands is the exact normalized water-leaving radiance,  $L_{WN}$ , which corresponds to the radiance vertically exiting from the water body just above the sea surface for the ideal case of the sun at the zenith and normalized by the atmospheric transmittance [2,4]. For each center wavelength,  $L_{WN}$  is retrieved from SeaPRISM measurements by standard NASA processing [13] and from the HyperSAS measurements by a new CCNY algorithm based on the same concepts as SeaPRISM data processing. Details on this data processing approach were already given by [15]. However, a summary is provided here to emphasize the physical considerations involved in this data processing approach, and to highlight the most important differences with the HyperSAS data processing approach.

The measured sea radiance  $L_T(\lambda, \theta, \varphi)$  can be decomposed into three components: (i) the radiance coming from the direct sun light reflected by the wavy sea surface (sun glint), (ii) the sea surface reflected radiance of the sky light (sky glint) and (iii) the water-leaving radiance emerging from the water body through the sea surface. The data processing detailed hereafter aims to retrieve the latter component from the total radiance measured from above water. In order to remove, or at least minimize, the impact of the sun glint on the measured sea radiance, the average  $L_T^*(\lambda, \theta, \varphi)$  is computed for a fixed percentage, typically 5%, of the  $N_T$  sea-radiance measurements exhibiting the lowest radiance levels [14,18]. In the case of HyperSAS,  $N_T$  is varying from 44 to 210 and two to 10 acquisitions are therefore used for the averaging. For the SeaPRISM system, a percentage of about 20% is taken because of the smaller number of acquisitions within a sequence. That corresponds to two acquisitions being retained out of  $N_T = 11$ . The sun glint radiance  $L_g$  can then be computed for a given solar zenith angle  $\theta_0$ , as follows:

$$L_g(\lambda, \theta_0, \theta, \varphi) = L_T(\lambda, \theta_0, \theta, \varphi) - L_T^*(\lambda, \theta_0, \theta, \varphi) \quad (1)$$

The water-leaving radiance  $L_W(\lambda, \theta, \varphi)$  is then computed as:

$$L_W(\lambda, \theta, \varphi) = L_T^*(\lambda, \theta, \varphi) - \rho(\theta_0, \theta, \varphi, w) L_s(\lambda, \theta', \varphi), \quad (2)$$

where the sky radiance,  $L_s(\lambda, \theta', \varphi)$ , is determined by simply averaging the  $N_i$  (3 for SeaPRISM and around 200 for HyperSAS) sky-radiance acquisitions. The coefficient  $\rho(\theta_0, \theta, \varphi, w)$  is the sea surface reflectance factor, which is dependent on sky condition, wind speed  $w$ , the solar zenith angle  $\theta_0$ , and the viewing geometry [21]. A recent study suggests that this factor can be adjusted spectrally [23]. But in this study, the spectrally flat values of  $\rho$ , computed based on the Hydrolight radiative transfer model [21], are

used. The impact of the potential spectral dependence is further discussed in the last part of this article. It should be mentioned that both sun and sky glint corrections are based on the Cox and Munk assumption to model the wind-ruffled sea surface [24], which remains questionable for these space and time scales [25]. However, a dedicated study by Hooker *et al.* [26] showed that the performance of that sun glint filtering is not noticeably perturbed by reducing the full-angle field of view (FAFOV) from 6° to 3° (HyperSAS). Nevertheless, it has been noted in this study that some of the above-water radiance values are shifted higher across all the channels when the FAFOV is reduced to 1.5°, which is similar to the SeaPRISM FAFOV of 1.2°; no explanation for the stepwise shift was found.

The exact water-leaving radiance  $L_{WN}(\lambda)$  is determined from  $L_W(\lambda, \theta, \varphi)$  as follows

$$L_{WN}(\lambda) = L_W(\lambda, \theta, \varphi) C_{\mathcal{R}Q}(\lambda, \theta_0, \theta, \varphi, \tau_a, IOP, w) \times C_{f/Q}(\lambda, \theta_0, \tau_a, IOP) [D^2 t_d(\lambda, \theta_0) \cos(\theta_0)]^{-1}, \quad (3)$$

where  $\tau_a$  and  $IOP$  stand for the aerosol optical thickness and the inherent optical properties, respectively.  $C_{\mathcal{R}Q}$  and  $C_{f/Q}$  are introduced to remove the dependence from the viewing geometry due to the refraction of wavy sea surface and the bidirectional effects in  $L_W(\lambda, \theta, \varphi)$ , respectively; the exact formulations of these terms can be found in [13], for example. In the HyperSAS and SeaPRISM processing both terms are interpolated from lookup tables produced for oceanic waters and from clear-sky conditions with  $\tau_a = 0.2$  at 550 nm, for various discrete  $\lambda$ ,  $\theta_0$ ,  $\theta$ ,  $\varphi$  and chlorophyll a concentration ( $Chl$ ) expressing  $IOP$  dependence [27]. The center wavelengths included in the lookup tables are 412.5, 442.5, 490, 510, 560, and 660 nm;  $C_{\mathcal{R}Q}$  and  $C_{f/Q}$  are then linearly interpolated or extrapolated for the specific wavelengths of HyperSAS or SeaPRISM systems.

The term  $D^2$  in (3) accounts for the variation of the sun-earth distance with the day of the year [28] in order to compute  $L_{WN}$  for the mean sun-earth distance. The last critically important term in (3) is the atmospheric transmittance  $t_d$ , equal to the sum of the direct and diffuse transmittances, and which is used in order to minimize the effect of the atmospheric radiation on the water-leaving radiance. The specific computation of this term is one of the most important differences between HyperSAS and SeaPRISM processing. In the NASA SeaPRISM processing, the transmittance  $t_{d\text{SeaPRISM}}$  is computed by the following empirical relationship [2,29]:

$$t_{d\text{SeaPRISM}}(\lambda, \theta_0) = \exp\left(-\frac{[0.5\tau_r(\lambda) + C_a\tau_a(\lambda) + \tau_{O3}(\lambda)]}{\cos\theta_0}\right), \quad (4)$$

where  $\tau_r$ ,  $\tau_a$ , and  $\tau_{O3}$  are the Rayleigh, aerosol and ozone optical thicknesses, respectively. The  $C_a$  coefficient accounts for aerosol phase function and



absorption properties and its value is typically around 0.14 with a slight spectral dependence. In the SeaPRISM processing,  $\tau_r$  is computed taking into account the atmospheric pressure variations,  $\tau_a$  is directly retrieved by the sun photometer component of the SeaPRISM measurements for each spectral band,  $\tau_{O_3}$  is computed from the total ozone mapping spectrometer (TOMS) dataset.

For the HyperSAS processing, the atmospheric transmittance  $t_{d\text{HyperSAS}}$  is directly computed from the irradiance measurements:

$$t_{d\text{HyperSAS}}(\lambda, \theta_0) = \frac{E_s(\lambda)}{D^2 \cos \theta_0 F_0(\lambda)}, \quad (5)$$

where  $F_0$  is the theoretical extraterrestrial solar irradiance for the mean sun-earth distance [30] and  $E_s$  is the mean value of the HyperSAS irradiance measurements over 3 min time acquisition.

### B. HyperSAS Data Quality Process

The final processing step consists in eliminating the data that is significantly corrupted by unexpected environmental effects or any stochastic artifacts. Such a quality assurance has already been developed for a SeaPRISM system in the framework of the AERONET-OC distribution. In particular, an automatic cloud screening based on almucantar and principal plane sky-radiance measurements [20] and an elimination of data showing negative value, or exceedingly high variance of measured radiances, are applied to generate quality-assurance level 1.5 products; see [13] for details. The SeaPRISM data of LISCO site used in this study are level 1.5 data, and have been manually checked, making sure that no corrupted spectra were present in this dataset. A specific data filtering procedure has been developed for HyperSAS, independently of SeaPRISM and is summarized below.

First, negative data are filtered and their values are replaced with zero, in the cases that the measurements are very close to the dark current value. Second, for each HyperSAS measurement sequence, the ratio of the downwelling irradiance  $E_s$  measured at 443 nm to its theoretical clear-sky value is computed. The theoretical irradiance is computed for the actual sun elevation with 6SV radiative transfer code [31] for an aerosol optical thickness of 0.1 at 550 nm, which is typically the situation in the LISCO location. Under totally, or even partially, overcast skies, the measured  $E_s$  drops down and the irradiance ratio departs from unity. On the basis of the distribution of the measured-to-computed  $E_s$  ratio [Fig. 2(a)] and following [12] the whole measurement sequence is eliminated from the data quality process if the ratio is outside the [0.85, 1.1] range. Note that the application of this filtering condition eliminates more than the half of the data as indicated by the rejection rate [Fig. 2(a)]. Third, the relative standard deviation of sky radiances  $L_s$  is computed for each measurement sequence. If the sky is partially cloudy, for instance, this standard deviation is enhanced by the progression of scattered clouds through the field-of-view of the sensor during the 3 min time acquisition. In order to filter the HyperSAS dataset for clear-sky conditions only, a relative standard deviation threshold of 5% has been set on the basis of the HyperSAS time series statistics [Fig. 2(b)].

All those previous filters are built on the basis of data quality checks of HyperSAS direct measurements. However, unexpected environmental effects can continue to exist even after this first data screening, and induce variable impacts on the final product throughout the whole data processing. Consequently, an independent filtering approach has been developed based on hyperspectral normalized water-leaving radiance  $L_{WN}$ . At the end of the HyperSAS processing any impact from sky and sun light should have been removed from the measured signal and

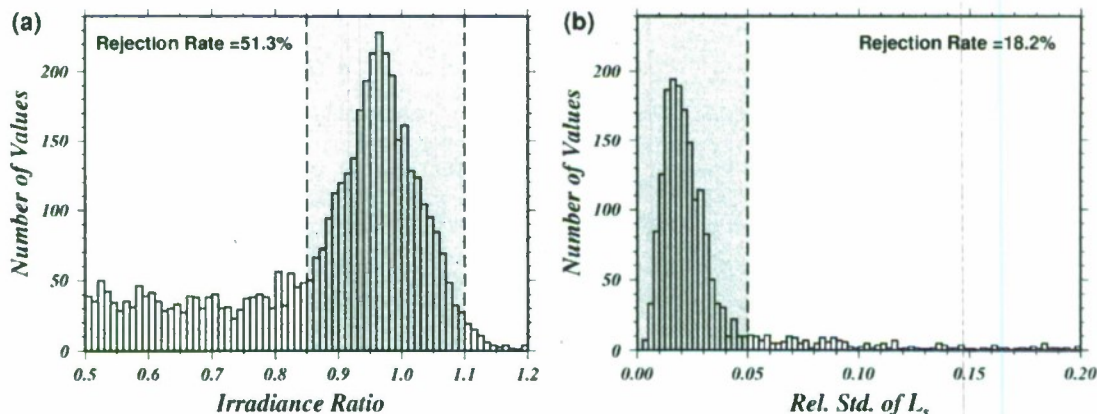


Fig. 2. (a) Histogram of the ratio of the irradiance  $E_s$  measured at 443 nm by HyperSAS to its theoretical clear-sky value computed from 6SV radiative transfer code. The value of this ratio must be between 0.85 and 1.1 (shaded area) for the corresponding data to be included in the data quality process. (b) Histogram of the relative standard deviation of sky radiances  $L_s$  having passed the  $E_s$  ratio filter. The values must be lower than 0.05 (shaded area) to pass the data quality process. Histograms and rejection rates have been established over the period from October 2009 to January 2011.



should be negligible in the retrieved  $L_{WN}$  spectrum. In the HyperSAS system spectral range, one of the most specific spectral patterns of the sky radiation field occurs around 760 nm where the atmospheric oxygen molecules exhibits a very strong absorption feature [32]. In Fig. 3(a), the oxygen absorption spectrum is plotted along with the average sun glint radiance  $L_g$  derived from the HyperSAS time series. It can be readily seen that the  $L_g$  spectrum shows a significant trough corresponding to the oxygen absorption peak, whereas the off-peak  $L_g$  values stay quite stable over this spectral region.

In order to assess whether or not the retrieved  $L_{WN}$  have been well-corrected for sun and sky glint radiances, two distinct spectral averages are computed as follows:

$$L_{WN}^{\text{on-peak}} = \frac{L_{WN}(760.2) + L_{WN}(763.6)}{2} \quad (6)$$

$$L_{WN}^{\text{off-peak}} = \frac{L_{WN}(753.6) + L_{WN}(756.9) + L_{WN}(770.2) + L_{WN}(773.6)}{4}, \quad (7)$$

where the values in parentheses are the wavelengths in nm corresponding to the current HyperSAS settings at the LISCO site. In the ideal case where all contamination by the sun and sky light reflected at the sea surface have been removed from the  $L_{WN}$ , the difference  $\Delta L_{WN} = L_{WN}^{\text{off-peak}} - L_{WN}^{\text{on-peak}}$  and the ratio of  $L_{WN}^{\text{off-peak}}$  over  $L_{WN}^{\text{on-peak}}$  must be close to 0 and 1, respectively. The histograms of these two quantities have been plotted in Figs. 3(b) and 3(c) for HyperSAS data that have successfully passed the first data quality check steps. From these statistics, it has been decided, based on a rejection rate of 20%, to eliminate any HyperSAS spectra from the data quality process if the difference  $\Delta L_{WN}$  is outside the range of  $[-0.01; 0.2] \text{ mW cm}^{-2} \text{ sr}^{-1} \mu\text{m}^{-1}$ , or if the  $L_{WN}$  ratio is outside the  $[-0.95; 1.2]$  interval. It is worth noting that this procedure makes it possible to ensure very low sun glint contamination for HyperSAS  $L_{WN}$  data retained.

#### 4. HyperSAS Intrinsic Uncertainty Assessment

A major difficulty with above-water measurements is associated with corrections of observations for the effect of surface waves that introduce significant fluctuations into the glint and reflected skylight components. These fluctuations induce different geophysical noise with respect to the sun position and viewing geometry [14]. Because HyperSAS and SeaPRISM do not have exactly the same viewing geometry throughout the day, it is of paramount importance to quantify the HyperSAS data quality

independently of SeaPRISM. After this initial quality assessment, it will then be possible to make use of HyperSAS and SeaPRISM time series measurements in order to cross-validate both systems.

##### A. Intrinsic Uncertainty Estimator

The data quality assessment of the HyperSAS system, along with its specific data processing procedure, is addressed here. First, HyperSAS data have been filtered based on the irradiance ratio and the sky-radiance variation filters, detailed above, to remove all data acquired during overcast conditions. It should be noted that the filters based on hyperspectral information have been relaxed for the analysis in this section, in order to first assess data quality even if strong sun and sky glint contaminations are present. Second, for each measurement sequence, the HyperSAS data processing procedure has been applied to  $N_T^*$  sea-radiance acquisitions separately, where  $N_T^*$  has been set to 20% of the  $N_T$

sea-radiance measurements exhibiting the lowest radiance levels. This elimination of the highest sea-radiances is equivalent to the effective removal of sun glint effects in the HyperSAS data processing. In addition, it is worth noting that  $N_T$  varies from 44 to 210 within a measurement sequence of three minutes because of the adjustment of the integration time to the target brightness. The value of 20% of  $N_T$  has been chosen, instead of 5% used in the standard sun glint correction of HyperSAS data, in order to increase the number of acquisition for each sequence, and make this analysis more statistically meaningful. Thus,  $N_T^*$  values of the exact normalized water-leaving radiance  $L_{WN}$  are retrieved for each HyperSAS measurement sequence, then an estimator of the relative standard deviation is calculated from the set of the individual  $L_{WN}(i)$  as follows:

$$\sigma_{\text{rel}} = \frac{1}{L_{WN}^{\text{est}}} \sqrt{\frac{1}{N_T^* - 1} \sum_{i=1}^{N_T^*} (L_{WN}(i) - L_{WN}^{\text{est}})^2}, \quad (8)$$

where  $L_{WN}^{\text{est}}$  is the exact normalized water-leaving radiance estimated by the operational HyperSAS processing based on the mean value of the sea radiance computed over the  $N_T^*$  individual measurements of each sequence. Thus, the value of  $\sigma_{\text{rel}}$  is an estimator of the uncertainties induced by the geophysical noise (i.e., environmental effects) and propagated through the whole data processing. This value is used to



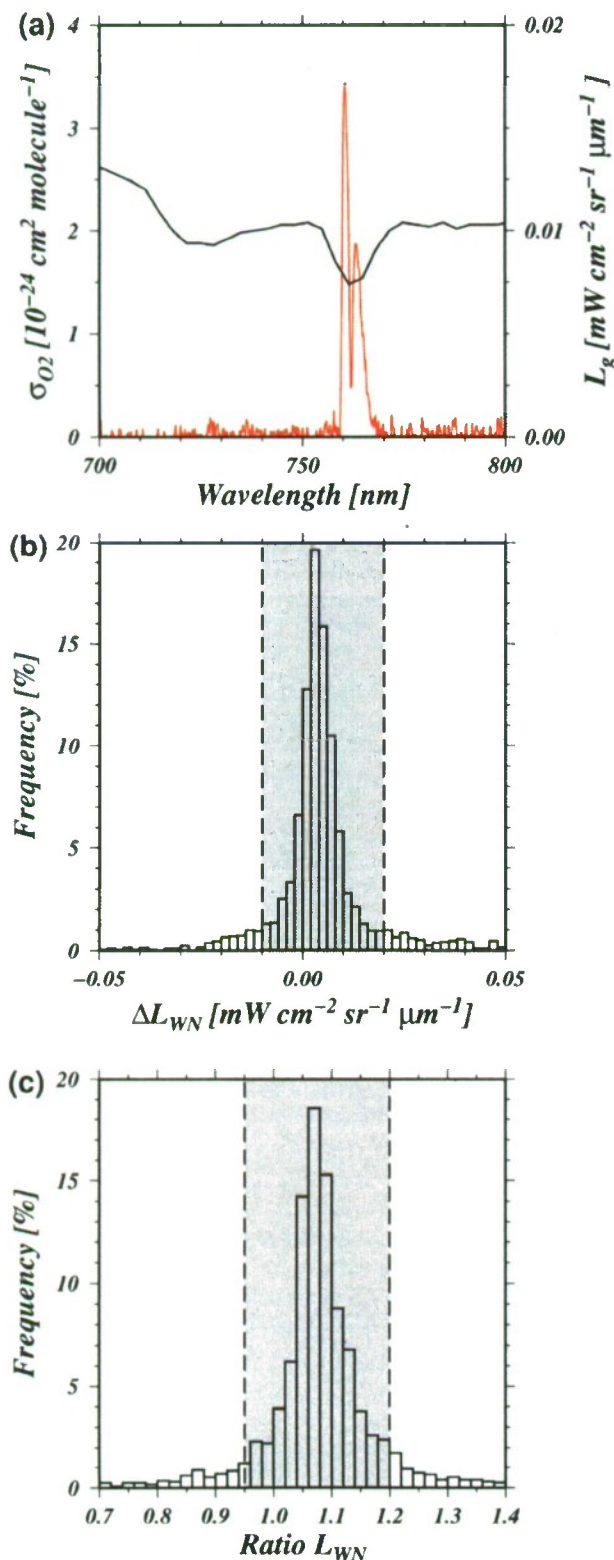


Fig. 3. (Color online) (a) Absorption cross section of oxygen,  $\sigma_{O_2}$ , in  $\text{cm}^2$  per molecule (red line, data from [32]) and average sun glint radiance  $L_g$  in  $\text{mW cm}^{-2} \text{ sr}^{-1} \mu\text{m}^{-1}$  derived from the HyperSAS dataset (black line). Histograms of (b) the difference and (c) the ratio of the normalized water-leaving radiances  $L_{WN}$  measured on and off the oxygen absorption peak centered on 760 nm. The shaded areas correspond to the range of acceptable values applied in the data quality process.

quantify the geophysical uncertainty associated with HyperSAS system.

#### B. HyperSAS Intrinsic Uncertainties

The parameter  $\sigma_{\text{rel}}$  has been computed for all the center wavelengths for all the measurement sequences for the different seasons of the year. The seasonal mean values of  $\sigma_{\text{rel}}$  are plotted in Fig. 4. The effect of the sun and sky light on the sea surface is primarily driven by the sun position in the sky and the wind-ruffled sea [33,34]. Because sun position and wind regimes change with the time of the year, (i.e., seasonally), the HyperSAS uncertainties are analyzed for each season independently. It should be noted that the time axis of the plots of Fig. 4 is given in UTC minus four hours as a local time indicator. In addition, a gray scale is used when  $\sigma_{\text{rel}}$  is lower than 5%, which is the required accuracy for water-leaving radiance remote sensing; a color scale is used otherwise.

In spring [Fig. 4(a)], the uncertainty estimator  $\sigma_{\text{rel}}$  at 550 nm is below 5% from early in the morning around 8:30 am up to 2:30 pm. After 3 pm, the impact of the sun glint is enhanced owing to the relative position of the sun to the radiance sensor. Consequently, the sun glint removal part of the data processing becomes ineffective, and  $\sigma_{\text{rel}}$  increases above 15% at 550 nm. It should also be noted that the relative uncertainties exhibit a spectral dependence. Thus, at 12 pm,  $\sigma_{\text{rel}}$  is lower than 5% over the whole spectral range from 340 to 740 nm. Outside this range and particularly in the near infrared part of the spectrum the uncertainties increase up to 8% at 800 nm and 30% at 860 nm. Over this specific part of the spectrum,  $L_{WN}$  is significantly low in comparison to the sky and sun radiances. As a result, the correction of the sea radiance from the wave induced reflected light is no longer accurate enough. Based on the statistics developed for the period April to July 2010 [Fig. 4(a)], the HyperSAS data quality can be summarized as follows: (i) uncertainties are below 5% for the spectral range of 330 to 750 nm until local noon, (ii) between 12 pm and 2 pm acceptable uncertainties are retrieved for a smaller spectral range, (iii) after 2:30 pm the contribution of the sun glint is strongly increasing and no data remain sufficiently accurate.

Regarding the summer period, the  $\sigma_{\text{rel}}$  values lead to quite similar conclusions. Nevertheless, it should be noted that the lack of data between 3:30 pm and 5 pm [Fig. 4(b)] results from the application of the sky-radiance relative standard deviation threshold in the data quality processing of HyperSAS. In fact, the sky-radiance sensor is pointing to the vicinity of the sun during this period. The measured sky radiance is consequently highly variable over the three minutes of the measurement sequence inducing a strong standard deviation similarly to that due to a scattered cloud passing through the sensor field of view. During fall and winter [Fig. 4(c) and 4(d)], the time range for accurate data is substantially



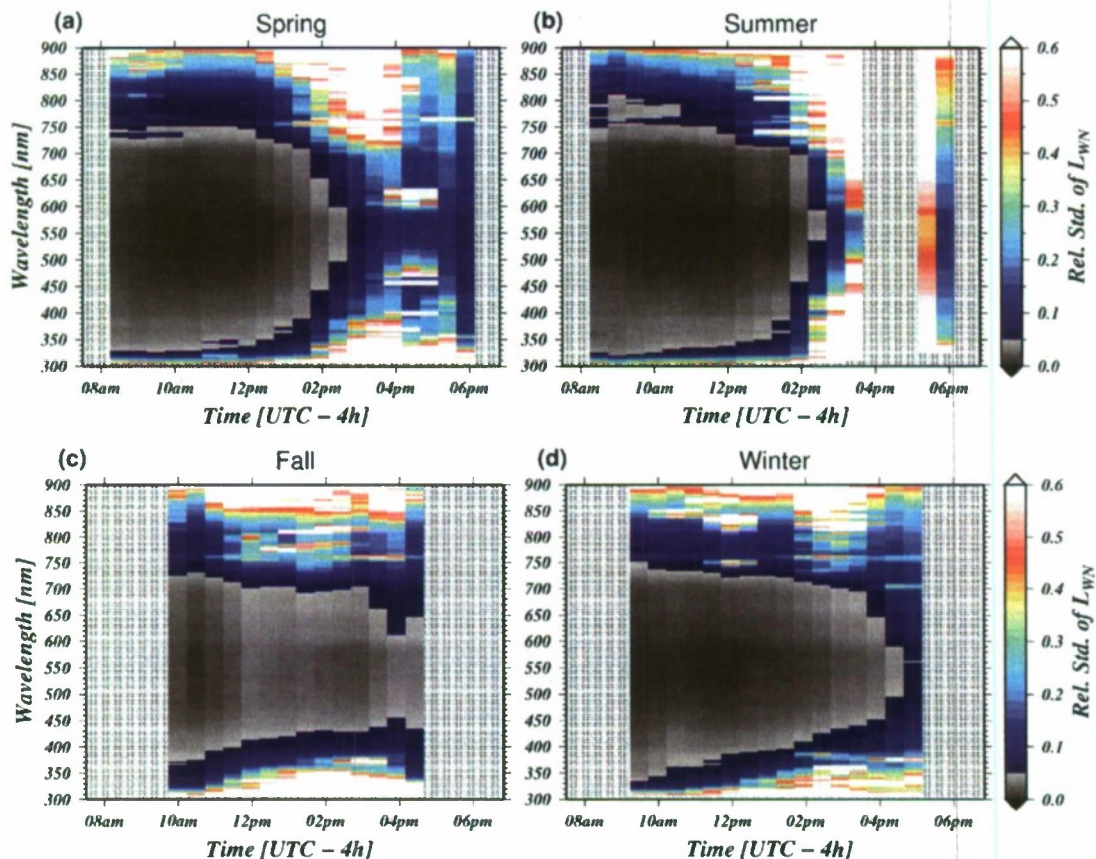


Fig. 4. (Color online) Relative standard deviation (Rel. Std.) of  $L_{WN}$  as retrieved by HyperSAS system displayed with respect to the time of acquisition and all the HyperSAS spectral bands. This relative standard deviation is used as an estimator of the intrinsic uncertainties of HyperSAS. A squared pattern is used when no data are available.

longer from around 9 am to 4:30 pm. However, the spectral range of the acceptable uncertainties is slightly reduced; especially in fall when this spectral range is limited to 420–690 nm on average.

A more synoptic view of HyperSAS intrinsic uncertainties can be expressed by plotting the mean  $\sigma_{rel}$  with respect to the viewing geometrical configuration. This configuration is totally described by the solar zenith angle and the relative azimuth  $\varphi$  between the sun and the sensor while the HyperSAS viewing angle is fixed and set to  $40^\circ$  from the nadir direction. The convention used for the relative azimuth is  $\varphi = 0^\circ$  when the sensor is in opposition to the sun, and  $\varphi = 180^\circ$  when the sun is behind the sensor. The results are displayed in Fig. 5 for three center wavelength widely used in ocean color radiometry applications: 443, 550 and 670 nm.

For these three bands, results show minimum uncertainties around  $\varphi = 130^\circ$ , which is consistent with previous theoretical studies [21]. The contamination by environmental effects of the retrieved  $L_{WN}$  becomes sensitive for  $\varphi < 60^\circ$  regardless of the sun elevation with uncertainties higher than 5%. As a consequence, it has been decided to eliminate from the HyperSAS data quality processing, all data taken for  $\varphi < 70^\circ$ . For the rest of the viewing configurations, the uncertainties remain lower than 5%,

thereby indicating the large range of viewing configuration available for acquiring accurate water-leaving radiance from above water. Furthermore, it should be noted that no data selection restrictions were made based on wind speed or sea state considerations for the results shown in Fig. 4. While the average data quality remains accurate, it can be concluded that the correction scheme of the sea surface effect is sufficiently accurate at the level of 5% uncertainty in  $L_{WN}$ . However, it should be remembered that potential biases affecting  $L_{WN}$  are not taken into account in this analysis, but will be assessed in the next section based on intercomparisons with the collocated SeaPRISM measurements. In conclusion, the significant HyperSAS data accuracy has been shown on the basis of statistics of daily measurements gathered over more than one year (i.e., October 2009 until January 2011), exhibiting uncertainties below 5% within consistent spectral and time ranges which are suitable for ocean color radiometry satellite validation activities.

## 5. SeaPRISM/HyperSAS Intercomparison

### A. Water-Leaving Radiance Qualitative Intercomparison

Based on the CCNY data processing, the exact water-leaving radiances,  $L_{WN}$ , are retrieved from the



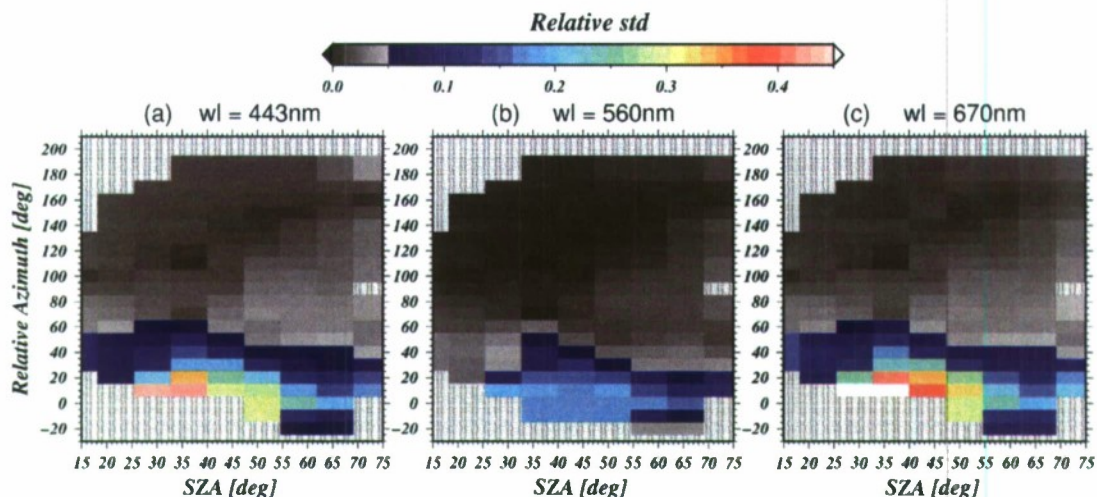


Fig. 5. (Color online) Relative standard deviation (uncertainty estimator) of  $L_{WN}$  as retrieved by HyperSAS system with respect to the solar zenith angle and the relative azimuth between the sun and the sensor (equal to  $180^\circ$  when the sun is behind the sensor) at (a) 443, (b) 560 and (c) 670 nm. A squared pattern is used when no data are available.

HyperSAS measurements over a more than one year period. SeaPRISM and HyperSAS data are compared assuming that both systems on the LISCO platform observe the same geophysical target, i.e., the same water composition, at the same time. As an example, the distributions of  $L_{WN}$  retrieved from SeaPRISM and HyperSAS measurements, respectively, are displayed for Nov. 4, 2009 (Fig. 6). This comparison shows a satisfactory spectral agreement between the two datasets. In addition, it should be noted that the hyperspectral data exhibit consistent supplementary information, in agreement with other datasets [35], showing specific fine spectral features not discernible in the multispectral  $L_{WN}$  data obtained from SeaPRISM.

The whole time series of  $L_{WN}$  at two SeaPRISM spectral bands are plotted in Fig. 7. Note that all the following intercomparisons are based on the level 1.5 SeaPRISM data and HyperSAS values derived from the complete quality check process for the time window between 9:00 and 16:00 LT. In addition, all

the HyperSAS values with a relative azimuth smaller than  $70^\circ$  have been eliminated because of the glint contamination as discussed in the previous section. For each day, the mean value and the standard variation are calculated for SeaPRISM and HyperSAS respectively, and plotted in Fig. 7.

In this figure, the time series exhibit strong seasonal variations for both datasets. For instance, a specific pattern of high water-leaving radiances is observable on March 17, 2010, resulting from an increase of sediment concentration following a significant storm event with higher riverine input and water body mixing. As a result, it can be concluded that the seasonal changes are captured well by the two above-water measurement systems over the 1-year datasets of collocated acquisitions at the LISCO site. This temporal agreement, combined with the spectral shape agreement of the LISCO data, qualitatively validates the concept and scientific consistency of measuring water-leaving radiance from above water in coastal water areas.

#### B. Direct Measurements Intercomparison

To further quantify the uncertainty of the  $L_{WN}$  obtained by above-water instrumentation, matchup intercomparisons were used for the whole set of data measured or obtained by SeaPRISM and HyperSAS systems. The intercomparisons were carried out for the five main SeaPRISM spectral bands, i.e., 413, 442, 491, 551 and 668 nm. The hyperspectral HyperSAS data were integrated with the sensor relative spectral response function of each SeaPRISM bands in order to produce equivalent data for both systems. The data involved were restricted to SeaPRISM measurement sequences taken within  $\pm 10$  min of HyperSAS sequence intervals. Since the sequence interval is 30 min for both systems, the intercomparisons were exclusively achieved between single sequences.

The statistical approach adopted here is associated with the consideration that neither SeaPRISM nor

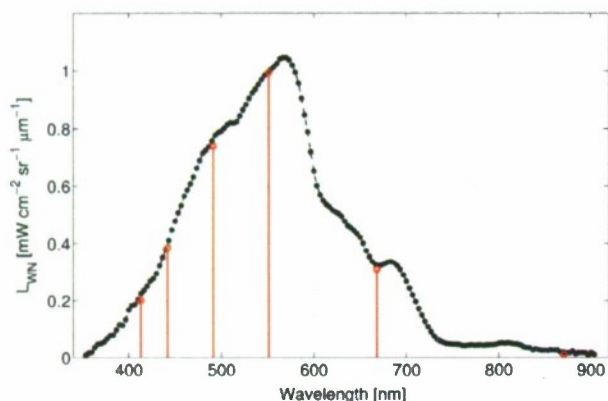


Fig. 6. (Color online) Examples of coincident HyperSAS (black dots) and SeaPRISM (red circles) exact normalized water-leaving radiance (in  $\text{mW cm}^{-2} \text{sr}^{-1} \mu\text{m}^{-1}$ ) for Nov. 4, 2009.



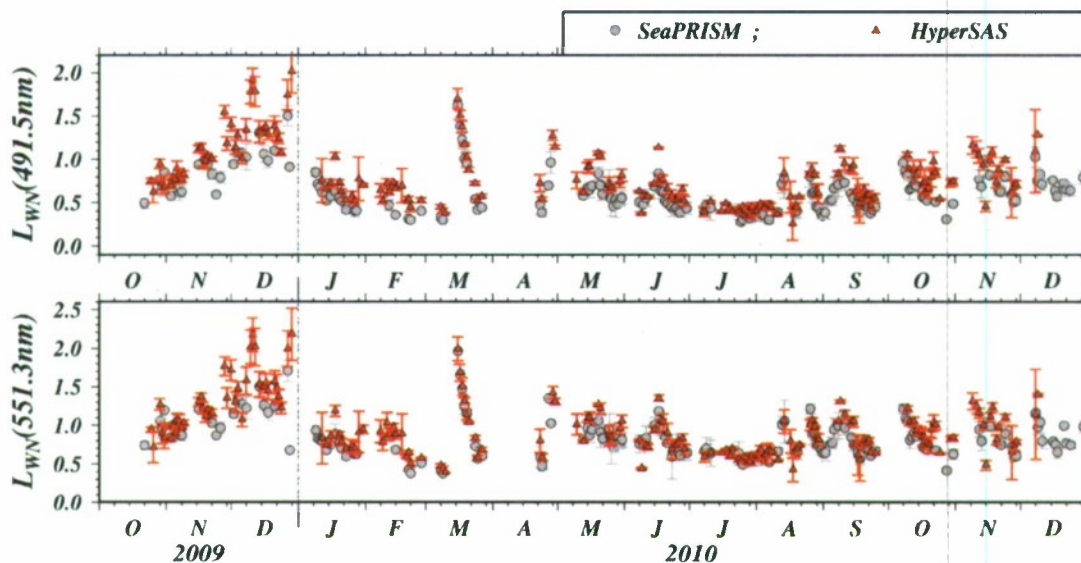


Fig. 7. (Color online) Time series of daily average of the exact normalized water-leaving radiance (in  $\text{mW cm}^{-2} \text{sr}^{-1} \mu\text{m}^{-1}$ ) retrieved with HyperSAS (red triangles) and SeaPRISM (gray circles) for two SeaPRISM bands centered on 551 and 491 nm. The vertical bars correspond to the daily standard deviations.

HyperSAS system can be assigned as the reference, since both systems are in above-water configuration. For this reason the intercomparisons were conducted using the unbiased relative percent difference (URPD) defined similarly to [14,18] as follows:

$$\text{URPD} = 200 \times \frac{1}{N} \sum_{i=1}^N \frac{y_i - x_i}{x_i + y_i}, \quad (9)$$

with  $x$  standing for SeaPRISM data and  $y$  for HyperSAS data and  $N$  being the number of matchup points available. Based on the same notation, the following bias was also used:

$$\text{bias} = \frac{1}{N} \sum_{i=1}^N y_i - x_i. \quad (10)$$

A least squares fit is also adjusted within the matchup points, with the associated coefficient of determination,  $R^2$ , and the equation of the regression line. It should be noted that no statistical filtering has been applied to the following intercomparisons to remove outliers.

The Figs. 8(a) and 8(b) show, respectively, the intercomparisons of direct measurements of the sky radiances  $L_s$  and the sea-radiance  $L_T$  averaged for each acquisition sequence. The two intercomparisons exhibit strong correlations between HyperSAS and SeaPRISM data with a coefficient of determination around 0.90 and 0.97 for sky and sea measurements, respectively. Note that no intercalibration has been applied to HyperSAS and SeaPRISM sensors that can contribute to the observed dispersion between the two datasets. However, the consistency between both systems is supported by the regression lines lying close to the 1:1 line for sea measurements.

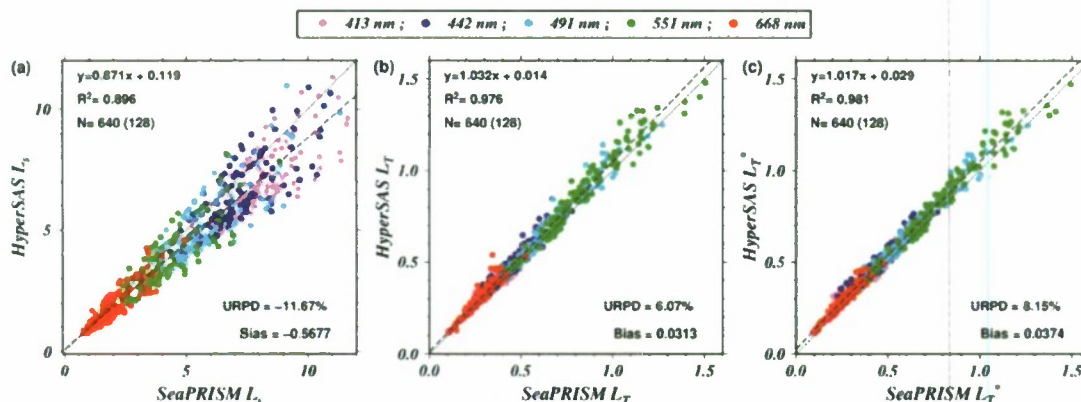


Fig. 8. (Color online) Intercomparisons of HyperSAS and SeaPRISM direct measurements (in  $\text{mW cm}^{-2} \text{sr}^{-1} \mu\text{m}^{-1}$ ) of (a) sky-radiance  $L_s$ , (b) total sea-radiance  $L_T$  and (c) the lowest sea-radiance values of each measurement sequence  $L_T^*$ .  $N$  is the total number of the comparison, the bracketed value is the number of different measurement sequences used in the comparison. The bias is given in radiance unit.



The coefficient of determination for the sky radiance is noticeably smaller than in the case of the sea radiance. That indicates a stronger dispersion of the  $L_s$  data in comparison to  $L_T$ , as can be readily discerned in Fig. 8. The  $L_s$  dispersion is decreasing with the increasing wavelengths as shown by the URPD values of Table 1, which is not the case for  $L_T$ . This higher dispersion is most likely due to the different viewing geometrical configurations between the two systems. Indeed,  $R^2$  of  $L_s$  comparison increases up to 0.99 for an URPD value smaller than 1.5% when the HyperSAS and SeaPRISM are close, more precisely when the data involved in the comparison are restricted to the HyperSAS sequences taken for an azimuth within  $\pm 5^\circ$  of the SeaPRISM azimuth. Note that the number of sequences for the comparison is far smaller with  $N = 11$  in this case. The  $L_s$  measurements therefore exhibit a higher sensitivity to the azimuth configuration than the  $L_T$  measurements. It should be remembered that  $L_s$  is subtracted from  $L_T$  after having been multiplied by the reflection factor  $\rho$  for obtaining the water-leaving radiance [sky glint removal, see Eq. (2)]. This highlights the importance of  $\rho$  in the data processing. The azimuth dependence of  $\rho$  has been implemented in HyperSAS data processing based on the same Hydrolight model that is used for SeaPRISM processing [21].

In the Fig. 8(c) the intercomparison of HyperSAS and SeaPRISM was carried out for the lowest values of the sea radiance, noted  $L_T^*$ . In this case, no significant variations of  $R^2$  are observed whatever the center wavelength in comparison to the  $L_T$  intercomparison (Table 1). This means that the first above-water data processing step, namely the sun glint removal, stays consistent regardless of the variable environmental conditions all along the year. However, the dispersion between the two datasets is increased by 2.1% on average in comparison with the  $L_T$  intercomparison as shown by the URPD values. This dispersion rise is significantly higher at the shorter wavelengths, with increases greater than 4% and 3% at 413 and 443 nm, respectively (Table 1). In addition, a slight positive bias is introduced by taking the minimum values of  $L_T$  as shown by the bias passing from 0.031 to 0.037 and the intercept

of the regression line from 0.014 to 0.029 between  $L_T$  and  $L_T^*$  intercomparisons. Assuming that HyperSAS and SeaPRISM point at the same spot with comparable sea surface conditions, the only differences between the two systems are integration time and field of view. The latter is higher for HyperSAS, with  $3^\circ$ , compared to SeaPRISM with  $1.2^\circ$ . Thus, the footprints of both sensors are a quasi-ellipse of  $0.68 \text{ m}^2$  and  $0.11 \text{ m}^2$  for HyperSAS and SeaPRISM, respectively. It can be argued that larger sensor field of view might very likely improve the sun glint removal step, particularly when long data time series, which include windy conditions, are considered. That is consistent with another study, which noticed that some of the above-water radiance values are shifted higher across all the channels when the field of view is reduced from  $3^\circ$  to  $1.5^\circ$  [26]. Also, the integration time of the SeaPRISM system is set to 75 ms. That is much shorter than the HyperSAS integration time, which is 2 s on average for the sea-radiance acquisitions. This considerable difference can also critically impact the efficacy of the sun glint removal step. Indeed, at a given viewing configuration, the sun glint variability arises from the wavelets orientation distribution whose statistics can be drastically changed by modifying spatial and time scales of the sensor acquisition [25,36]. It is believed that only a dedicated study would be able to objectively define the best combination of field of view and integration time to be used in above-water measurements in calm or windy conditions. This present study, which is limited to uncertainty quantification, highlights that these features can be a significant source of bias especially at the shorter wavelengths for combinations of narrow sensor footprints and short integration times, as is the case for SeaPRISM at the LISCO site.

### C. Sources of Uncertainty

Using the direct measurements of HyperSAS or SeaPRISM, several data processing steps are applied to obtain the exact normalized water-leaving radiance as described in Section 3. The uncertainties generated by each of these steps are analyzed here by means of intercomparisons over the whole LISCO data acquisition period. The first step corresponds

Table 1. Summary of HyperSAS and SeaPRISM Direct Measurement Intercomparison Over One Year Period at LISCO Site Corresponding to 128 Coincident Measurement Sequences

Parameter		Wavelength (nm)					Spectral Average
		413	442	491	551	668	
$L_s$	$R^2$	0.69	0.70	0.71	0.73	0.77	0.92
	Regression line	$0.86x + 0.05$	$0.89x + 0.12$	$0.86x + 0.20$	$0.86x + 0.14$	$0.90x + 0.03$	$0.87x + 0.12$
	URPD	-14.7	-10.6	-11.4	-11.6	-10.1	-11.7
$L_T$	$R^2$	0.90	0.92	0.95	0.95	0.90	0.98
	Regression line	$0.98x + 0.03$	$1.04x + 0.01$	$1.04x + 0.01$	$1.05x + 0.00$	$1.13x - 0.01$	$1.03 + 0.01$
	URPD	4.2	7.2	4.9	4.3	9.7	6.1
$L_T^*$	$R^2$	0.90	0.93	0.96	0.96	0.93	0.98
	Regression line	$0.90x + 0.07$	$0.99x + 0.05$	$0.96x + 0.03$	$1.03x + 0.02$	$1.08x + 0.01$	$1.02x + 0.03$
	URPD	8.0	10.3	6.0	4.9	11.5	8.2



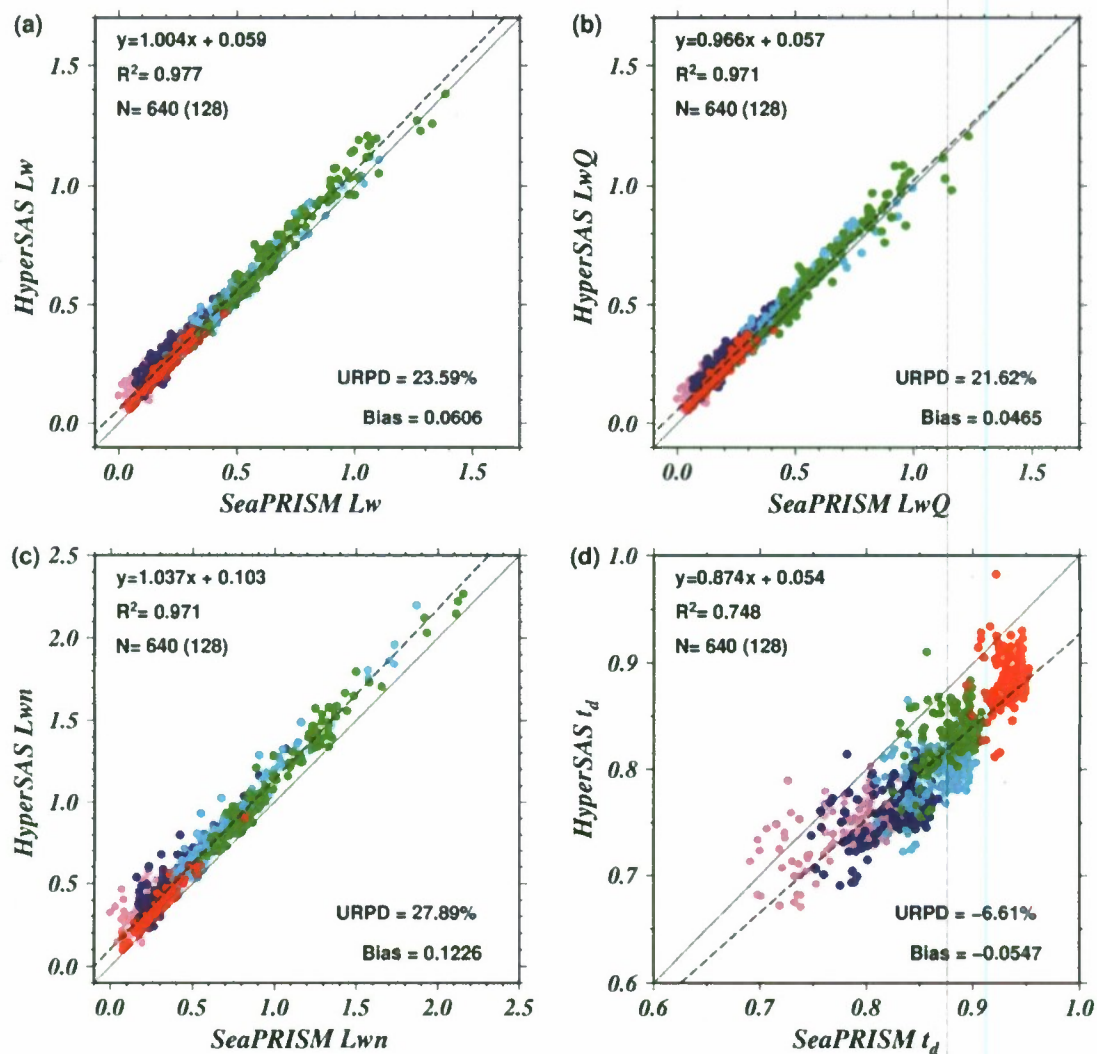


Fig. 9. (Color online) Intercomparisons of HyperSAS and SeaPRISM intermediate product: (a) the water-leaving radiance  $L_w$  (in  $\text{mW cm}^{-2} \text{sr}^{-1} \mu\text{m}^{-1}$ ), (b) the water-leaving radiance corrected for the viewing angle dependency  $L_wQ$  (in  $\text{mW cm}^{-2} \text{sr}^{-1} \mu\text{m}^{-1}$ ), (c) the water-leaving radiance corrected for the atmospheric transmittance  $L_{wn}$  (in  $\text{mW cm}^{-2} \text{sr}^{-1} \mu\text{m}^{-1}$ ) and (d) the atmospheric transmittance  $t_d$ . The same color convention as in Fig. 8 is used.

to the sky glint removal, see Eq. (2), to obtain the water-leaving radiance  $L_w$ . The  $L_w$  values derived from HyperSAS and SeaPRISM are compared in Fig. 9(a). Both datasets are well correlated with a

coefficient of determination  $R^2 = 0.98$  averaging over the spectral range. The values of  $R^2$  for the different center wavelengths are close to the average value, although slightly lower, especially at 413 nm where

Table 2. Similar to Table 1 but for the Water-Leaving Radiance  $L_w$ , the Water-Leaving Radiance Corrected for the Viewing Angle Dependency  $L_wQ$  and the Water-Leaving Radiance Corrected for the Atmospheric Transmittance  $L_{wn}$

Parameter		Wavelength (nm)					Spectral Average
		413	442	491	551	668	
$L_w$	$R^2$	0.78	0.90	0.96	0.96	0.94	0.98
	Regression line	$0.95x + 0.08$	$1.01x + 0.07$	$1.01x + 0.06$	$1.03x + 0.04$	$1.07x + 0.02$	$1.00x + 0.06$
	URPD	47.1	30.2	13.2	8.3	19.0	23.6
$L_wQ$	$R^2$	0.80	0.90	0.96	0.95	0.94	0.97
	Regression line	$0.96x + 0.07$	$1.01x + 0.06$	$0.99x + 0.05$	$1.00x + 0.03$	$1.07x + 0.02$	$0.97x + 0.06$
	URPD	46.6	28.9	10.5	4.5	17.5	21.6
$L_{wn}$	$R^2$	0.66	0.87	0.96	0.97	0.94	0.97
	Regression line	$0.92x + 0.15$	$1.06x + 0.13$	$1.08x + 0.09$	$1.03x + 0.09$	$1.07x + 0.04$	$1.04x + 0.10$
	URPD	49.7	36.0	19.9	11.8	22.0	27.9



$R^2 = 0.78$  (Table 2). Moreover, a significant positive bias is produced corresponding to an absolute value of  $0.023 \text{ mW cm}^{-2} \text{ sr}^{-1} \mu\text{m}^{-1}$  in comparison to  $L_T^*$  case. Thus, this first step induces an increase in dispersion corresponding to the addition of approximately 15% in URPD values when compared with the  $L_T^*$  sea-radiance intercomparison of Fig. 8(c). This drastic rise in the URPD values is mostly driven by the sky glint removal step at the shorter wavelengths producing URPD increases of 39% and 20% at 413 and 442 nm, respectively. This degradation of the SeaPRISM-HyperSAS consistency can be explained, at least partly, by the increase toward the shorter wavelengths of the relative importance of the sky-radiance  $L_s$  to the sea-radiance  $L_T$  and the dispersion induced by the previous sun glint removal processing step. This issue is discussed further below.

When the water-leaving radiance is corrected for viewing angle dependence, this product being denoted by  $LwQ$ , the dispersion is reduced by almost 2% URPD, while the bias decreases from 0.061 to  $0.046 \text{ mW cm}^{-2} \text{ sr}^{-1} \mu\text{m}^{-1}$  [Fig. 9(b)]. The spectral URPD values in Table 2 span a range from 4.5% at 551 nm, where the water-leaving signal is high, up to 46.6% at 413 nm, where the water-leaving signal is low, because of the high absorption by turbid LISCO waters, as well as the large dispersion induced by the sun and sky glint removal steps. Intermediate values of URPD were observed to decrease monotonically with increasing water-leaving intensities. It is worth noting that comparable URPD (or equivalent) values have been retrieved by other independent studies comparing coincident sets of below and above-water measurements [18,26] for the blue-green, green and red bands, namely 491, 551 and 668 nm. However, the URPD values retrieved in this study at 413 and 442 nm are significantly higher than those of the other cited studies. In the last section of this paper, we identify and address sources of uncertainty at shorter wavelengths and examine means of reducing them.

Another important intermediate product, denoted as  $Lwn$ , is the water-leaving radiance normalized by the cosine of the solar zenith angle and the atmospheric transmittance,  $\cos \theta_0 t_d$ , (though not adjusted for viewing angle dependence or for the effects of the nonisotropic distribution of the in-water light field). It should be remembered that this normalization step is the most important difference between HyperSAS or SeaPRISM data processing. Indeed, for HyperSAS, the atmospheric transmittance is directly derived from the downwelling irradiance measurement, whereas for SeaPRISM it is obtained by parameterization of the respective optical thicknesses of air molecules, aerosols and ozone. The values of  $Lwn$  derived from HyperSAS or SeaPRISM measurements are compared in Fig. 9(c) and in Table 2. Although the two datasets stay strongly correlated, the dispersion increases by 4.3% in URPD values, in comparison to the  $Lw$  case. Note that this dispersion value is close to the absolute value of URPD

retrieved for the atmospheric transmittance  $t_d$  intercomparison shown in Fig. 9(d), which clarifies the cause and effect relationship. The SeaPRISM parameterization of the atmospheric transmittance is limited to a two-dimensional ideal atmosphere, which cannot encompass the full range of environmental variability in the atmospheric attenuation (e.g., surrounding clouds, water vapor spatial distribution) contrary to what is done with the downwelling irradiance measurements of HyperSAS. As a result, the SeaPRISM parameterization ceases to be sufficiently efficient for certain environmental conditions impacting on both dispersion and bias in the intercomparison. Since the normalization by  $\cos \theta_0 t_d$  is a critical step for obtaining  $L_{WN}$  values suitable for satellite validation, a dedicated study is needed to further analyze the impact of using direct measurements of the atmospheric transmittance (HyperSAS) instead of through parameterization based on the optical thickness data (SeaPRISM) and use its results to propose improvements in approach.

The impact of the successive processing steps on the retrieval uncertainties can be summarized as follows: (i) the sun glint removal step generates unbiased uncertainties of about 2.1%, with a positive bias in HyperSAS data, (ii) the sky glint removal step generates unbiased uncertainties of about 15% which is particularly critical at the shorter wavelengths, (iii) the viewing angle dependence correction improves the data intercomparison by reducing the unbiased uncertainties by about 2%, (iv) the atmospheric effect normalization generates 4.3% of unbiased uncertainties, and induces a nonnegligible bias, especially at the shorter wavelengths, due most likely to an insufficiently accurate atmospheric transmittance derivation in the SeaPRISM processing. Finally, the exact normalized water-leaving radiances are then retrieved with an overall uncertainty of 26% and a positive bias of about  $0.09 \text{ mW cm}^{-2} \text{ sr}^{-1} \mu\text{m}^{-1}$  for HyperSAS data (Fig. 10). Spectrally, the smallest uncertainty, about 8.4%, occurs at 551 nm, where the water-leaving signal is

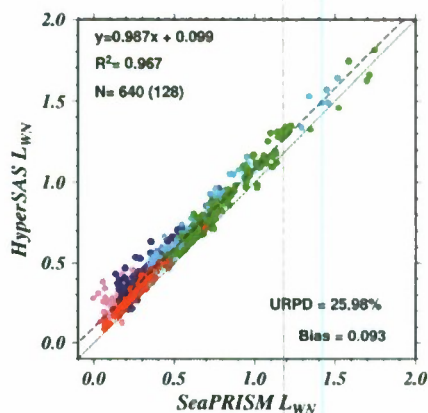


Fig. 10. (Color online) Intercomparison of the exact normalized water-leaving radiances (in  $\text{mW cm}^{-2} \text{ sr}^{-1} \mu\text{m}^{-1}$ ) derived from SeaPRISM and HyperSAS measurements. The same color convention as in Fig. 8 is used.



Table 3. Similar to Table 1 but for the Exact Normalized Water-Leaving Radiance  $L_{WN}$  Derived from HyperSAS and SeaPRISM Measurements

Parameter		Wavelength (nm)					Spectral Average
		413	442	491	551	668	
LWN	R2	0.70	0.89	0.97	0.96	0.95	0.97
	Regression line	$0.92x + 0.13$	$1.04x + 0.11$	$1.03x + 0.09$	$0.98x + 0.09$	$1.04x + 0.04$	$0.99x + 0.10$
	URPD	49.0	34.7	17.2	8.4	20.6	26.0

large in comparison to the atmospheric contribution (see Table 3). This uncertainty increases with decreasing water-leaving signal with an URPD value of about 20% at 668 nm and greater than 30% in the extreme blue part of the spectrum. In spite of these uncertainties, the HyperSAS and SeaPRISM datasets are strongly correlated for the central wavelengths from 442 to 668 nm ( $R^2 > 0.9$ ) and to a lesser extent for the 413 nm band ( $R^2 > 0.7$ ) with the slope of the regression lines close to one (Table 3). Based on this result, it can be concluded that the LISCO data provided by collocated above-water instrumentations are statistically satisfactory correlated. However, a strong bias persists between the two datasets preventing attainment of an acceptable uncertainty budget of 5% required for satellite validation purposes [37]. Consequently, further efforts are needed to improve the above-water data processing so as to reduce the sources of uncertainty identified above.

#### D. Assessment of Possible Improvements in the Data Processing

The uncertainty budget, as established based on LISCO data, originates from differences in data processing for the two collocated radiometer systems. This needs to be improved in order to reconcile the two measured datasets. It has been underlined herein, that the atmospheric transmittance normalization step leads to an increase in the data dispersion by about 4% on average. In order to minimize the impact of this step, the SeaPRISM data has been processed using the respective HyperSAS atmospheric transmittance values to normalize the

water-leaving radiance. The product obtained in this way is denoted as  $L'_{WN}$ . Replacing the standard SeaPRISM  $L_{WN}$  by  $L'_{WN}$  in the LISCO data intercomparison [Fig. 11(a)] diminishes the bias from  $\sim 0.09$  down to  $\sim 0.06 \text{ mW cm}^{-2} \text{ sr}^{-1} \mu\text{m}^{-1}$ . At the same time, the corresponding URPD values decrease by about 6.5%, which is consistent with discrepancies induced by the dispersion observed in the atmospheric transmittance intercomparison shown in the Fig. 9(d). The regression line stays the same as previously, with an offset of  $\sim 0.1$ , indicating higher bias and dispersion at the shorter wavelengths. That is confirmed by the spectral URPD values, shown in the Table 4, ranging from 2.8% at 551 nm up to 44.4% at 413 nm. Thus, improvements in the atmospheric transmittance derivation by SeaPRISM can significantly enhance data accuracy, especially in the blue-green part of the spectrum where URPD values are divided by a factor greater than two. However, the use of a common atmospheric transmittance for both the HyperSAS and SeaPRISM data processing failed to remove, or at least reduce, the bias at the shorter wavelengths, i.e., 413 and 491 nm, leaving unacceptable data discrepancies for satellite data validation purposes.

It has been shown in Subsection 5.B that the sun glint removal step contributes significantly to the observed discrepancies between SeaPRISM and HyperSAS data, and in a more pronounced way at the shorter wavelengths. Furthermore, it has been highlighted that the extremely narrow SeaPRISM footprint on the sea surface may critically impact the statistics of wavelet orientation and hence subsequently the sun glint proportion contained in the

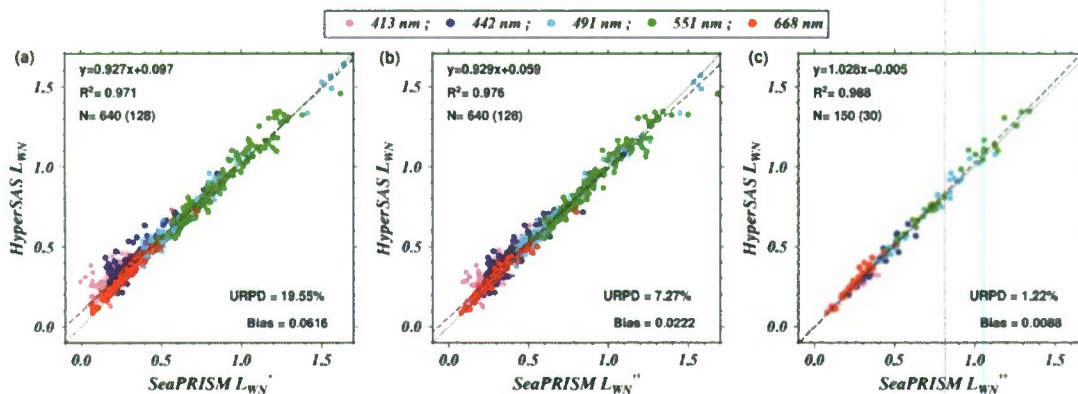


Fig. 11. (Color online) Same as Fig. 10 for the comparison of HyperSAS  $L_{WN}$  with (a)  $L'_{WN}$ , the water-leaving radiance derived from SeaPRISM measurements by replacing the SeaPRISM atmospheric transmittance by the HyperSAS one, (b) the water-leaving radiance  $L''_{WN}$  derived from SeaPRISM measurement by using  $L_T$  instead of  $L'_T$ , and (c)  $L'''_{WN}$  for a restricted HyperSAS-SeaPRISM relative azimuth range (see text for details).



Table 4. Similar to Table 1 but for the Data Plotted Fig. 11

Parameter		Wavelength (nm)					Spectral Average
		413	442	491	551	668	
$L_{WN}'$	R2	0.71	0.91	0.98	0.96	0.95	0.97
	Regression line	$0.87x + 0.13$	$0.97x + 0.11$	$0.96x + 0.08$	$0.93x + 0.09$	$1.00x + 0.04$	$0.93x + 0.10$
$L_{WN}''$	URPD	44.4	26.7	8.42	2.84	15.4	19.6
	R2	0.73	0.91	0.98	0.96	0.95	0.98
	Regression line	$0.92x + 0.07$	$0.96x + 0.06$	$0.95x + 0.05$	$0.91x + 0.08$	$0.94x + 0.03$	$0.93x + 0.06$
	URPD	17.1	11.3	2.5	-1.0	6.4	7.3
$L_{WN}''$ for a restricted azimuth range	R2	0.91	0.94	0.97	0.98	0.95	0.99
	Regression line	$0.90x + 0.02$	$1.01x + 0.00$	$1.02x + 0.00$	$1.03x + 0.00$	$1.07x + 0.00$	$1.03x + 0.00$
	URPD	-3.2	-0.4	1.6	2.6	5.4	1.2

measured sea radiances. In order to quantify the impact of this on the SeaPRISM uncertainty budget, the overall SeaPRISM data processing has been run without the sun glint removal step which amounts to deriving the water-leaving radiance from the mean value instead of the minimum value of the measured sea radiances of each acquisition sequence. The resulting product denoted as  $L_{WN}''$  is thus obtained when the appropriate HyperSAS atmospheric transmittance is used in place of the SeaPRISM one and  $L_t$  is used instead of  $L_t^*$ . This resulting modified SeaPRISM product is compared to the standard HyperSAS water-leaving radiance in the Fig. 11(b). This modification in the SeaPRISM data processing induces a significant decrease in the bias, changing from 0.062 down to 0.022  $\text{mW cm}^{-2} \text{sr}^{-1} \mu\text{m}^{-1}$ . This is accompanied by severe reduction of the URPD value, which decreases by  $\sim 12\%$  resulting in a spectrally averaged URPD of 7.3%. The spectral URPD values are thus effectively reduced by a factor greater than two for all SeaPRISM bands. However, the slope of the regression line is unchanged and stays close to 0.93 for an offset of 0.06, thereby indicating stronger discrepancies especially for low radiance and at shorter wavelengths.

In the Fig. 11(c), the intercomparison results based on the  $L_{WN}''$  have been plotted for a restricted range of SeaPRISM azimuths, spanning  $\pm 10^\circ$  of those of HyperSAS in the Fig. 11(c). This limitation in azimuth range permits minimization of the impact of both the bidirectionality dependence and the differences in the surface-reflected radiance contributions to the water-leaving radiance derivations from HyperSAS and SeaPRISM datasets. After that data filtering, only 30 points of coincident data remain for intercomparison. However, the coefficient of determination now shows a stronger correlation between the two datasets, with  $R^2 = 0.99$ , which is particularly sensitive at the 413 nm band (Table 4). The average URPD value is reduced down to 1.2% and the spectral URPD values are lower than 5% in absolute value even at the shortest wavelengths. Furthermore, the slope of the regression line is closer to 1 ( $=1.03$ ) than before ( $=0.93$ ) and the associated offset turned out to be negligible ( $<0.01$  in absolute

value) as well as the overall bias equal to  $0.009 \text{ mW cm}^{-2} \text{sr}^{-1} \mu\text{m}^{-1}$ .

To summarize, a satisfactory matching between HyperSAS and SeaPRISM datasets is reached after the following modifications in the standard SeaPRISM processing: (i) replacement of the SeaPRISM atmospheric transmittance by that derived from the irradiance measurements of the HyperSAS system; (ii) skipping the sun glint removal step; and (iii) reducing the HyperSAS viewing configuration to a range closer to that of SeaPRISM. The recognition of the last two factors makes it possible, without any instrumentation change, to improve the consistency of the two datasets to a level suitable for validation of ocean color radiometry satellite data. It can therefore reasonably be concluded that the sun glint removal step and correction for the directional effects (i.e., the corrections for sky glint and bidirectionality of the water-leaving radiance) need to be significantly improved.

The correction for bidirectionality is currently done using a bidirectional reflectance distribution function (BRDF) based on open ocean water assumptions [4,13] where backscattering and absorption of water particulates are functions of only one parameter, the chlorophyll concentration [Chl]. These assumptions are usually not valid in coastal waters. This can create significant errors in BRDF estimations in coastal zones [38,39]. However, a complete analysis of the appropriateness and impact of the BRDF used is far beyond the scope of this article and can be considered as a second order correction compared to the sun glint removal issues. The sky glint correction is also sensitive to directional effects, as has been shown above. In current data processing, this correction makes use of theoretical modeling of the sea surface based on a Gaussian distribution of the wave and wavelet orientations [21,24]. However, as we have seen, the sun glint removal step can skew the statistics of wave orientation distribution, particularly by taking the minimum value of the sea-radiance measurement sequence [25]. Therefore, an important part of inaccuracies induced by the sky glint correction might be seen as a consequence of the preceding step in the SeaPRISM data processing. The sun glint correction, which is the very first



step of the above-water data processing, is most likely the main source of uncertainty since any error done at this step would be amplified through the whole processing.

The consistency of the sun glint radiances,  $L_g$ , retrieved by HyperSAS and SeaPRISM is evaluated below.  $L_g$  values have been computed following Eq. (1) of Section 3 from the SeaPRISM and HyperSAS data at LISCO site and the level 2.0 AERONET-OC data of the following sites: Venice with Acqua Alta Oceanographic Tower (AAOT) (N45°19'; E12°30'), Palgrunden (N58°45'; E13°09'), Gustaf Dalen Lighthouse Tower (GDLT) (N58°35'; E17°28') and Martha's Vineyard Coastal Observatory MVCO (N41°18'; W70°33'). These sites were selected because they cover more than three consecutive years of data acquisition and different kinds of water properties going from clear to very turbid waters [13]. They also cover a large range of sensor altitude from 10 m for AAOT and MVCO up to 49 m for Palgrunden. For all these datasets, the sun glint radiances have been averaged over their respective time period and have been plotted with respect to the wavelength in the Fig. 12(a). Differences of the sun glint radiance observed from site to site are mainly driven by the wind speed annual conditions and the value of the maximum solar elevation of the year, which is dependent on the latitude of the site location. However, notwithstanding the absolute value of  $L_g$ , the spectral shape of the sun glint radiance is observed to be conserved regardless of the AERONET-OC site considered. For instance, the AERONET-OC  $L_g$  measured at LISCO site is progressively decreasing from  $3.4 \times 10^{-2}$  at 413 nm to  $0.9 \times 10^{-2} \text{ mW cm}^{-2} \text{ sr}^{-1} \mu\text{m}^{-1}$  in the red part of the spectrum. In contrast,  $L_g$  measured by the collocated HyperSAS system is roughly bell-shaped with values ranging from 1.5 to  $2.8 \text{ mW cm}^{-2} \text{ sr}^{-1} \mu\text{m}^{-1}$  between 413 and 551 nm, and then decreasing down to  $1.6 \text{ mW cm}^{-2} \text{ sr}^{-1} \mu\text{m}^{-1}$  at 668 nm; the same value is conserved at 870 nm. Those different spectral shapes of  $L_g$  derived from SeaPRISM and HyperSAS can be readily discerned in Fig. 12(a). It is worth noting that SeaPRISM and HyperSAS  $L_g$  exhibit a good agreement in the green and red parts of the spectrum but significant discrepancies appear at the shorter wavelengths. That point is consistent with the respective discrepancies in the normalized water-leaving radiance intercomparison attributed to differences in the sun glint correction step as shown above.

The sun glint component of the upwelling radiance results from the specular reflection on the sea surface of the direct incoming sun light [40]. The refraction at the sea surface depends only on the wave state of the sea surface and on the index of refraction of the water and can consequently be assumed spectrally invariant [21]. Thus, the sun glint radiance  $L_g$  must be strictly proportional to the direct solar irradiance incoming at the sea surface, which can be expressed at a given wavelength  $\lambda$ , see [29] for example, as follows:

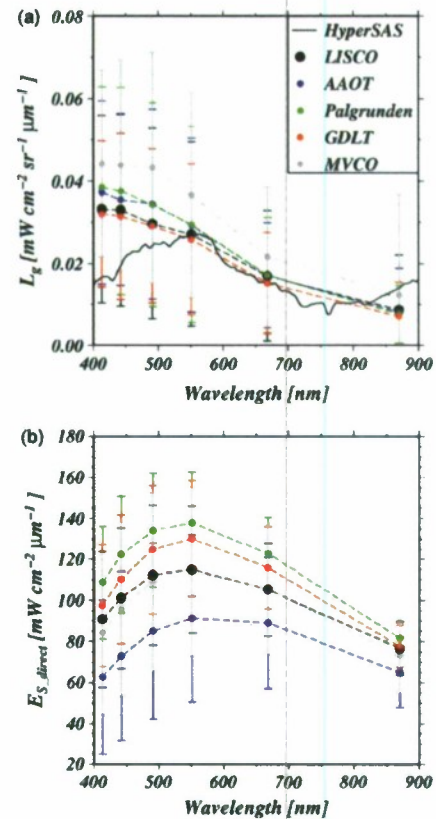


Fig. 12. (Color online) (a) Average of the sun glint contribution to the sea radiance (in  $\text{mW cm}^{-2} \text{ sr}^{-1} \mu\text{m}^{-1}$ ) derived from the HyperSAS (black line) and SeaPRISM (black dots) at LISCO site, and the following AERONET-OC sites (data level 2.0): AAOT (blue dots), Palgrunden (green dots), GDLT (red dots) and MVCO (gray dots). (b) Incoming direct solar irradiance at the sea surface (in  $\text{mW cm}^{-2} \text{ sr}^{-1} \mu\text{m}^{-1}$ ) calculated from the above-listed AERONET sites data. The vertical bars correspond to plus or minus the standard deviation calculated over the whole time series of each dataset.

$$E_{s, \text{direct}}(\lambda) = \exp\left(-\frac{\tau_r(\lambda) + \tau_a(\lambda) + \tau_{\text{gaz}}(\lambda)}{\cos \theta_0}\right) F_0(\lambda), \quad (11)$$

where the first term of the right-hand side of the equation corresponds to the direct atmospheric transmission as a function of the Rayleigh ( $\tau_r$ ), aerosol ( $\tau_a$ ), and gaseous absorption ( $\tau_{\text{gaz}}$ ) optical thicknesses, and the cosine of the solar zenith angle,  $\theta_0$ . It should be noted that the values of these parameters are directly accessible via the AERONET data distribution [20]. The term  $F_0$  is the extraterrestrial solar irradiance [30]. The mean value of  $E_{s, \text{direct}}$  derived from the datasets of each selected AERONET-OC site is plotted with respect to the wavelength in the Fig. 12(b). The spectral shapes of  $E_{s, \text{direct}}$  are equivalent for all the AERONET-OC sites with a steep increase from 413 to 551 nm followed by a smooth decrease toward the red part of the spectrum. Offsets are however clearly visible between the different datasets, but they certainly originate from differences in the typical atmospheric parameters and latitude of the sites. The



sun glint radiances derived from the SeaPRISM system of the different AERONET-OC sites possess a significantly different spectral behavior than the expected one, as exhibited by the  $E_{s\_direct}$  spectral shapes. Indeed, the SeaPRISM sun glint radiances are still increasing toward the shorter wavelength from 551 nm contrary to the  $E_{s\_direct}$  spectra. In contrast, the HyperSAS sun glint radiances at the LISCO site exhibit spectral shape in much better conformity to  $E_{s\_direct}$ , showing increasing values from 413 to 551 nm before reaching a maximum and decreasing toward the longer wavelengths.

Thus, the HyperSAS sun glint radiance is qualitatively consistent with the expected spectral shape of the sun glint component at the shorter wavelengths. That is not the case for the SeaPRISM retrievals. It can be concluded that the application of the current sun glint correction step to the SeaPRISM system leads to overcorrect the data in the blue part of the spectrum. This can be understood as follows. First, the sky radiation increases exponentially toward the shorter wavelengths, making the differences between the bright and shadowed facets of the waves more pronounced. Consequently, a significant part of the sky glint is probably (unintentionally) removed by the sun glint correction step from the SeaPRISM sea radiance. Then, when the actual sky glint correction is applied to these "sun glint" corrected data, the resulting water-leaving radiance data will be overcorrected for sky glint removal. This overcorrection will be, once again, more pronounced in the blue part of the spectrum, given that the sky radiance is normally higher for the (blue) shorter wavelengths. This sun glint overcorrection of the SeaPRISM data can also explain the bias and dispersion in the SeaPRISM/HyperSAS intercomparison resulting in URPD values reaching 47%, 30% and 13% at 413, 442 and 491 nm, respectively (see Section 5.C). Thus, the current sun glint correction procedure remains a major source of uncertainty for the 413, 442 and 491 nm bands of SeaPRISM. Improvements, along these lines, for these procedures would represent major accomplishments for drastically reducing the uncertainties of SeaPRISM data and would surely enhance the data quality of the necessary ground-truth information provided by the AERONET-OC network for validation of the ocean color radiometry satellite data.

## 6. Summary and Conclusion

The focus of this study was primarily to assess the validity of collocated above-water multi and hyperspectral radiometric instrumentation to accurately measure the water-leaving radiance with a view to support validation activities for satellite derived parameters in coastal areas. Multispectral SeaPRISM and hyperspectral HyperSAS instrumentations were detailed, as well as the water quality at the LISCO location. The exact normalized water-leaving radiance retrieval algorithm used for hyperspectral measurements has been specifically

described, highlighting the differences between multi and hyperspectral system processing. A data quality process, based on the hyperspectral information, has been developed for the HyperSAS system. This permits filtering out sun and sky glint contaminated data, as well as overcast conditions. HyperSAS data quality was first quantified independently of SeaPRISM by propagating the variability of measurements through the whole HyperSAS data processing procedure. It has been shown that the intrinsic uncertainties of those data are lower than 5% for a large spectral range, namely from 340 to 740 nm, and for a seasonally dependent time range, and more specifically to the sun elevation at the solar noon. In addition, the HyperSAS intrinsic uncertainties are shown to be lower than 5% when the relative azimuth is greater than 60° regardless of the solar zenith angle. Consequently, it has been decided to restrict the HyperSAS quality-checked products to the data acquired for relative azimuth greater than 70°.

Over a more than one year period, LISCO data were qualitatively validated on the basis of the temporal and spectral shape agreement of the retrieved normalized water-leaving radiances. Then, the two datasets were quantitatively analyzed using match-up intercomparisons. The impact of the successive data processing steps on the retrieval uncertainties was quantified. This intercomparison exercise showed that the sun and sky glint removal steps generate strong unbiased uncertainties of about 2% and 15%, respectively, as well as a significant bias. The different ways of deriving the atmospheric transmittance used for HyperSAS and SeaPRISM systems is responsible for about 4% of unbiased uncertainties and for an important bias especially at the shorter wavelengths. Eventually, the overall uncertainty of the retrieved exact normalized water-leaving radiances ranges from 8% at 551 nm to 49% at 413 nm for a spectral average of 26%. However, the HyperSAS and SeaPRISM datasets are strongly correlated for the central wavelengths from 442 to 668 nm ( $R^2 > 0.93$ ) and to a lesser extent for the 413 nm band ( $R^2 > 0.76$ ) with the slope of the regression lines close to 1.

The viewing angle dependence correction step improves data intercomparison by reducing the unbiased uncertainties by 2% and the absolute bias by more than  $0.01 \text{ mW cm}^{-2} \text{ sr}^{-1} \mu\text{m}^{-1}$ . Although this step permits achievement of significant data standardization enhancements, this correction is currently being done using bidirectionality functions modeled for open ocean rather than coastal optical properties. Thus, additional improvement can very probably be expected through the use of a bidirectionality correction adapted to moderately turbid coastal waters.

Other directions to be followed for improving the SeaPRISM data processing have been delineated in the last part of this article. First, it has been shown that improvements of the SeaPRISM atmospheric transmittance retrieval can reduce dispersion and



lead to important enhancements in data quality. Second, the sun glint removal step has been shown to generally overcorrect the SeaPRISM data, and thereby skew the wave structure statistics used for the sky glint correction part. In turn, the sky glint removal step overcorrects the SeaPRISM data for the surface effects. That is particularly critical at the shorter wavelengths. It has been shown that the unbiased relative percentage difference with HyperSAS is significantly reduced with a new value close to 1% for normalized water-leaving radiances when no sun glint correction is applied to the SeaPRISM data.

Significant improvements for the sky glint correction step are expected by refining the calculation of water surface reflection based on improved statistics of wave structures that are more appropriate for the space and time scales considered [25], and adjusting the reflection parameters for the spectral variation of the downwelling sky-radiance distribution, which is sensitive to both aerosol loading and type [23]. Importantly, however, it has been shown in this study that the main part of the uncertainties due to the sky glint correction step results from the improper correction for the sun glint signal. It appears that the related discrepancies arise from differences in the sensor exposure (integration) time and fields of view (i.e., variations in the observed target footprint) inducing variations of the statistics of the wave configuration distribution. These impact the sun glint or wave shadowing component in the measurements of sea radiance. Therefore revisiting the sun glint determination in the SeaPRISM processing is strongly recommended, to make sure that sun and sky glint correction steps are properly decoupled. In this context, the spectral shape of the retrieved sun glint radiance provides information on the accuracy of the sun glint correction. This spectral information can then be used to filter SeaPRISM data even more efficiently. As to the HyperSAS system, the sun and sky glint correction can very likely be improved thanks to the polarization measurements being made at the LISCO site following existing procedures of surface effect minimization [17,41]. Test and validation of these new techniques and correction algorithms will be possible and achievable in the near future, based on datasets from collocated HyperSAS and SeaPRISM systems at LISCO.

In conclusion, the consistency between HyperSAS and SeaPRISM data retrievals has been demonstrated over one whole year of measurements for varying environmental conditions, including strong winds. The different sources of uncertainty of the above-water radiometric measurements have been quantitatively identified, enhancing the prospects for future refinements in data processing. Furthermore, the demonstrated consistency of HyperSAS data expands the suitability of the LISCO site as a calibration/validation site, making it possible to contemplate the wider use of LISCO for monitoring current and future ocean color multispectral satellites as the Visible/Infrared Imager Radiometer Suite or

the Ocean Land Colour Instrument, regardless of spectral band characteristics, as well as for other hyperspectral satellite missions, as the Hyperspectral Imager for the Coastal Ocean.

This work was partially supported by grants from the Office of Naval Research (ONR) and the National Oceanographic and Atmospheric Administration. We would like to thank NASA AERONET team for SeaPRISM calibration, data processing and support of the site operations. Special thanks go to the principal investigators of the AERONET-OC sites for managing and maintaining both instrumentation and data distribution. We are grateful to Dr. G. Zibordi for frequent advice during the installation of the SeaPRISM and for data processing insights, as well as to Emmanuelle Cluset and Marius Canini from CIMEL Electronique. André Morel and Bernard Gentili are thanked for providing the look-up tables for bidirectional correction. The authors would also like to thank the reviewers for their relevant comments and suggestions, which we believe greatly enhanced the quality of the paper.

## References

1. IOCCG, "Why ocean colour? The societal benefits of ocean-colour technology," in *Reports of the International Ocean-Colour Coordinating Group*, T. Platt, N. Hoepffner, V. Stuart, and C. Brown, eds. (IOCCG, 2008).
2. H. R. Gordon and D. K. Clark, "Clear water radiances for atmospheric correction of coastal zone color scanner imagery," *Appl. Opt.* **20**, 4175–4180 (1981).
3. J. L. Mueller, A. Morel, R. Frouin, C. Davis, R. Arnone, K. Carder, Z. P. Lee, R. G. Steward, S. Hooker, C. D. Mobley, S. McLean, B. Holben, M. Miller, C. Pietras, K. D. Knobelspiesse, G. S. Fargion, J. Porter, and K. Voss, "Ocean optics protocols for satellite ocean color sensor validation, Revision 4, Vol. III: Radiometric measurements and data analysis protocols," NASA/TM-2003-211621, (NASA, 2003).
4. A. Morel and B. Gentili, "Diffuse reflectance of oceanic waters. III. Implication of bidirectionality for the remote-sensing problem," *Appl. Opt.* **35**, 4850–4862 (1996).
5. H. R. Gordon, "Atmospheric correction of ocean color imagery in the Earth Observing System era," *J. Geophys. Res.* **102**, 17081–17106 (1997).
6. K. G. Ruddick, F. Ovidio, and M. Rijkeboer, "Atmospheric correction of SeaWiFS imagery for turbid coastal and inland waters," *Appl. Opt.* **39**, 897–912 (2000).
7. P. J. Werdell, B. A. Franz, and S. W. Bailey, "Evaluation of shortwave infrared atmospheric correction for ocean color remote sensing of Chesapeake Bay," *Remote Sens. Environ.* **114**, 2238–2247 (2010).
8. M. H. Wang and H. R. Gordon, "Calibration of ocean color scanners: how much error is acceptable in the near infrared?" *Remote Sens. Environ.* **82**, 497–504 (2002).
9. B. A. Franz, S. W. Bailey, P. J. Werdell, and C. R. McClain, "Sensor-independent approach to the vicarious calibration of satellite ocean color radiometry," *Appl. Opt.* **46**, 5068–5082 (2007).
10. S. W. Bailey and P. J. Werdell, "A multi-sensor approach for the on-orbit validation of ocean color satellite data products," *Remote Sens. Environ.* **102**, 12–23 (2006).
11. D. K. Clark, M. A. Yarbrough, M. E. Feinholz, S. Flora, W. Broenkow, Y. S. Kim, B. C. Johnson, S. W. Brown, M. Yuen, and J. L. Mueller, "MOBY, a radiometric buoy for performance monitoring and vicarious calibration of satellite ocean color



- sensors: Measurement and data analysis protocols," in *Ocean Optics Protocols for Satellite Ocean Color Sensor Validation*, Revision (NASA, 2003).
12. D. Antoine, F. d'Ortenzio, S. B. Hooker, G. Bécu, B. Gentili, D. Tailliez, and A. J. Scott, "Assessment of uncertainty in the ocean reflectance determined by three satellite ocean color sensors (MERIS, SeaWiFS and MODIS-A) at an offshore site in the Mediterranean Sea (BOUSSOLE project)," *J. Geophys. Res.* **113**, C07013 (2008).
13. G. Zibordi, B. N. Holben, I. Slutsker, D. Giles, D. D'Alimonte, F. Mélin, J. F. Berthon, D. Vandemark, H. Feng, and G. Schuster, "AERONET-OC: a network for the validation of ocean color primary radiometric products," *J. Atmos. Ocean. Technol.* **26**, 1634–1651 (2009).
14. S. B. Hooker, G. Lazin, G. Zibordi, and S. McLean, "An evaluation of above-and in-water methods for determining water-leaving radiances," *J. Atmos. Ocean. Technol.* **19**, 486–515 (2002).
15. G. Zibordi, F. Mélin, S. B. Hooker, D. D'Alimonte, and B. Holben, "An autonomous above-water system for the validation of ocean color radiance data," *IEEE Trans. Geosci. Remote Sens.* **42**, 401–415 (2004).
16. S. Hlaing, T. Harmel, A. Ibrahim, I. Ioannou, A. Tonizzo, A. Gilerson, and S. Ahmed, "Validation of ocean color satellite sensors using coastal observational platform in Long Island Sound," *Proc. SPIE* **7825**, 782504 (2010).
17. A. Tonizzo, T. Harmel, A. Ibrahim, S. Hlaing, I. Ioannou, A. Gilerson, J. Chowdhary, B. Gross, F. Moshary, and S. Ahmed, "Sensitivity of the above water polarized reflectance to the water composition," *Proc. SPIE* **7825**, 78250F (2010).
18. G. Zibordi, S. B. Hooker, J. F. Berthon, and D. D'Alimonte, "Autonomous above-water radiance measurements from an offshore platform: a field assessment experiment," *J. Atmos. Ocean. Technol.* **19**, 808–819 (2002).
19. D. A. Aurin, H. M. Dierssen, M. S. Twardowski, and C. S. Roesler, "Optical complexity in Long Island Sound and implications for coastal ocean color remote sensing," *J. Geophys. Res.* **115**, C07011 (2010).
20. B. N. Holben, T. F. Eek, I. Slutsker, D. Tanre, J. P. Buis, A. Setzer, E. Vermote, J. A. Reagan, Y. J. Kaufman, and T. Nakajima, "AERONET-A federated instrument network and data archive for aerosol characterization," *Remote Sens. Environ.* **66**, 1–16 (1998).
21. C. D. Mobley, "Estimation of the remote-sensing reflectance from above-surface measurements," *Appl. Opt.* **38**, 7442–7455 (1999).
22. O. Dubovik and M. D. King, "A flexible inversion algorithm for retrieval of aerosol optical properties from sun and sky radiance measurements," *J. Geophys. Res.* **105**, 20673–20696 (2000).
23. Z. P. Lee, Y. H. Ahn, C. Mobley, and R. Arnone, "Removal of surface-reflected light for the measurement of remote-sensing reflectance from an above-surface platform," *Opt. Express* **18**, 26313–26324 (2010).
24. C. Cox and W. Munk, "Statistics of the sea surface derived from sun glitter," *J. Mar. Res.* **13**, 198–227 (1954).
25. S. Kay, J. D. Hedley, and S. Lavender, "Sun glint correction of high and low spatial resolution images of aquatic scenes: a review of methods for visible and near-infrared wavelengths," *Rem. Sens.* **1**, 697–730 (2009).
26. S. B. Hooker, G. Zibordi, J. F. Berthon, and J. W. Brown, "Above-water radiometry in shallow coastal waters," *Appl. Opt.* **43**, 4254–4268 (2004).
27. A. Morel, D. Antoine, and B. Gentili, "Bidirectional reflectance of oceanic waters: accounting for Raman emission and varying particle scattering phase function," *Appl. Opt.* **41**, 6289–6306 (2002).
28. G. W. Paltridge and C. M. R. Platt, *Radiative Processes in Meteorology and Climatology* (Elsevier, 1977).
29. D. Tanre, M. Herman, P. Y. Deschamps, and A. Deleffe, "Atmospheric modeling for space measurements of ground reflectances, including bidirectional properties," *Appl. Opt.* **18**, 3587–3594 (1979).
30. G. Thuillier, M. Herse, D. Labs, T. Foujols, W. Peetermans, D. Gillotay, P. C. Simon, and H. Mandel, "The solar spectral irradiance from 200 to 2400 nm as measured by the SOLSPEC spectrometer from the ATLAS and EURECA missions," *Sol. Phys.* **214**, 1–22 (2003).
31. S. Y. Kotchenova, E. F. Vermote, R. Matarrese, and F. J. Klemm, "Validation of a vector version of the 6S radiative transfer code for atmospheric correction of satellite data. Part I: Path radiance," *Appl. Opt.* **45**, 6762–6774 (2006).
32. K. Bogumil, J. Orphal, T. Homann, S. Voigt, P. Spietz, O. C. Fleischmann, A. Vogel, M. Hartmann, H. Kromminga, and H. Bovensmann, "Measurements of molecular absorption spectra with the SCIAMACHY pre-flight model: instrument characterization and reference data for atmospheric remote-sensing in the 230–2380 nm region," *J. Photochem. Photobiol. A Chem.* **157**, 167–184 (2003).
33. C. Cox and W. Munk, "Measurement of the roughness of the sea surface from photographs of the sun's glitter," *J. Opt. Soc. Am.* **44**, 838–850 (1954).
34. T. Nakajima and M. Tanaka, "Effect of wind-generated waves on the transfer of solar radiation in the atmosphere-ocean system," *J. Quant. Spectrosc. Radiat. Transfer* **29**, 521–537 (1983).
35. Z. Lee, K. L. Carder, S. K. Hawes, R. G. Steward, T. G. Peacock, and C. O. Davis, "Model for interpretation of hyperspectral remote-sensing reflectance," *Appl. Opt.* **33**, 5721–5732 (1994).
36. E. J. Hochberg, S. Andrefouet, and M. R. Tyler, "Sea surface correction of high spatial resolution Ikonos images to improve bottom mapping in near-shore environments," *IEEE Trans. Geosci. Remote Sens.* **41**, 1724–1729 (2003).
37. IOCCG, "Minimum requirements for an operational, ocean-colour sensor for the open ocean," in *Reports of the International Ocean Colour Coordinating Group, No 1*, A. Morel, ed. (IOCCG, 1997).
38. Y.-J. Park and K. Ruddick, "Model of remote-sensing reflectance including bidirectional effects for case 1 and case 2 waters," *Appl. Opt.* **44**, 1236–1249 (2005).
39. Z. P. Lee, K. Du, K. J. Voss, G. Zibordi, B. Lubac, R. Arnone, and A. Weidemann, "An inherent-optical-property-centered approach to correct the angular effects in water-leaving radiance," *Appl. Opt.* **50**, 3155–3167 (2011).
40. G. W. Kattawar and C. N. Adams, "Stokes vector calculations of the submarine light field in an atmosphere-ocean with scattering according to a Rayleigh phase matrix: effect of interface refractive index on radiance and polarization," *Limnol. Oceanogr.* **34**, 1453–1472 (1989).
41. B. Fougnie, R. Frouin, P. Lecomte, and P. Y. Deschamps, "Reduction of skylight reflection effects in the above-water measurement of diffuse marine reflectance," *Appl. Opt.* **38**, 3844–3856 (1999).